

# Numerical simulation of drop and bubble dynamics with soluble surfactant

Qiming Wang <sup>\*</sup>, Michael Siegel <sup>†</sup>, and Michael R. Booty <sup>†</sup>

*<sup>\*</sup> Department of Mathematics and Statistics,*

*York University, Toronto, Ontario M3J 1P3, Canada and*

*<sup>†</sup> Department of Mathematical Sciences and Center for Applied Mathematics and Statistics,*

*New Jersey Institute of Technology,*

*University Heights, Newark, NJ 07102, USA*

## Abstract

Numerical computations are presented to study the effect of soluble surfactant on the deformation and breakup of an axisymmetric drop or bubble stretched by an imposed linear strain flow in a viscous fluid. At the high values of bulk Peclet number  $Pe$  in typical fluid-surfactant systems, there is a thin transition layer near the interface in which the surfactant concentration varies rapidly. The large surfactant gradients are resolved using a fast and accurate ‘hybrid’ numerical method that incorporates a separate, singular perturbation analysis of the dynamics in the transition layer into a full numerical solution of the free boundary problem. The method is used to investigate the dependence of drop deformation on parameters that characterize surfactant solubility. We also compute resolved examples of tipstreaming, and investigate its dependence on parameters such as flow rate and bulk surfactant concentration.

PACS numbers:

## I. INTRODUCTION

Surfactants, or surface-active agents, can significantly alter interfacial evolution and flow in a two-phase fluid mixture by changing the surface tension. A notable example is the phenomenon of tipstreaming, in which a thin thread and small droplets are emitted from the tip of a drop or bubble that is stretched in an extensional flow. Tipstreaming was first observed by G. I. Taylor in his pioneering four-roller mill experiments [39], although the phenomenon has only recently been attributed to the presence of surfactant. Surfactants are also commonly used as emulsifiers, detergents, foaming or wetting agents. A thorough description of their properties and applications is given in [14].

This paper focuses on the effect of soluble surfactant on the deformation and breakup of a single drop or bubble stretched by an extensional flow in a viscous fluid. With and without surfactant, this canonical problem has been a subject of much study since Taylor's initial investigations. Experimental studies that include controlled addition of specific surfactants have been given by De Bruijn [12] and Janssen, Boon, and Agterof [19], [20]. The tipstreaming observed in these studies motivated Anna and Meyer [3] to utilize soluble surfactant in a microfluidic device to create submicron droplets. In the experiments, an elongational flow draws a separate fluid phase from the orifice of a capillary tube and focuses its tip, stretching the interface and causing a gradient of surfactant concentration along it. Under the right conditions, surfactants are adsorbed to the interface from the bulk fluid and cannot desorb fast enough compared to their rate of compression along it so that the tip becomes highly packed with surfactant [29]. This leads to a greatly reduced surface tension and a highly curved tip with a strong Marangoni stress [6], [40]. When its surfactant concentration is large enough, the highly curved tip is drawn via the Marangoni stress into a thin thread, which subsequently breaks into very small surfactant-laden droplets. The same mechanism applies to tipstreaming that is produced in other geometries. The phenomenon has been proposed as a way to produce micron-sized, monodisperse droplets for use in applications.

Most numerical studies of the effect of surfactant on the deformation and breakup of a single bubble or drop in extensional flow are for surfactant that is insoluble, that is, confined to the interface alone. Under the simplification of low Reynolds number flow, the evolution can be described completely by interface quantities and solved by surface-based methods such as the boundary integral method. This is among the most accurate and efficient numerical

methods for solving free and moving boundary problems.

Boundary integral simulations of the effect of insoluble surfactant on the deformation and breakup of axisymmetric and 3D drops in an imposed flow have been given by Stone and Leal [38], Milliken, Stone and Leal [28], Bazhlekov, Anderson, and Meijer [5], and Eggleton and Stebe [17]. These characterize the dependence of drop deformation on the capillary number  $Ca = \mu_2 GR_0/\gamma_0$ , where  $\mu_2$  is the suspending fluid viscosity,  $G$  is the imposed strain rate,  $R_0$  is the undeformed radius of the drop, and  $\gamma_0$  is the surface tension of a clean interface. Tipstreaming is observed in the boundary integral computations of Bazhlekov, Anderson, and Meijer [5], and Eggleton et al. [17] when the ratio  $\lambda = \mu_1/\mu_2$  of drop to suspending fluid viscosity is small and the capillary number is above a critical value. To the best of our knowledge, these are the only numerical simulations that evoke the tipstreaming observed in experiments. Other boundary integral studies of drop and bubble evolution with insoluble surfactant are, e.g., [24], [22], [33], [35], [42], [48]. Volume of fluid numerical simulations [13], [34] of low viscosity ratio drops with insoluble surfactant in extensional flow also show droplets or small drop fragments emitted from pointed bubble ends. However, these are on the scale of the mesh spacing and are therefore not well resolved, so that tipstreaming may have been introduced as a numerical artifact.

A soluble surfactant advects and diffuses in the bulk fluid, and there is an exchange or transfer between its dissolved form in the bulk and its adsorbed form on the interface. We adapt a ‘hybrid’ numerical method for the study of surfactant solubility effects in interfacial flow that was introduced in [7], [47]. The method applies for small bulk diffusion of surfactant, or equivalently for large bulk Peclet number  $Pe$ . The value of  $Pe$  in typical systems is  $10^5$  to  $10^6$  or higher [9], and at these high values there is a narrow transition layer adjacent to the interface in which bulk surfactant concentration gradients are large. The method incorporates a singular perturbation analysis of the dynamics in the transition layer into a full numerical solution of the interfacial free boundary problem. Away from the transition layer, the bulk concentration is taken to be spatially uniform and effectively diffusion-free. A key to the success of this formulation is that a highly accurate boundary integral method can be adapted to solve the full moving boundary problem, including the influence of surfactant solubility. Without the special large  $Pe$  treatment this and other surface-based methods would not easily apply. The accuracy and efficiency of the hybrid method was demonstrated in [7] by comparison with a traditional numerical approach that uses finite differences on a

curvilinear coordinate mesh, without the transition layer reduction.

Several improvements or refinements of the hybrid numerical method have been implemented for this study. These include an extension to axisymmetric geometry, the use of a more general, mixed-kinetic boundary condition for the bulk surfactant concentration  $C$  at the interface, and a new far-field or matching condition for  $C$  that better resolves the structure of the transition layer.

Other numerical studies of soluble surfactant dynamics, which employ either artificially small  $Pe$  or finely adapted grids are, e.g., [10], [18], [21], [25], [27], [41], [30], [43], [45], [50]. Eggleton and Stebe [16] numerically investigate drop deformation in an extensional flow in the ‘sorption-controlled’ limit (see §II A). Their model allows surfactant to adsorb and desorb from the interface, but ignores changes in the bulk concentration from its uniform, equilibrium far-field value, which are negligible in this limit.

We use the hybrid method to characterize the dependence of drop deformation on the capillary number and parameters that are relevant or specific to surfactant solubility. The influence of solubility is generally to reduce gradients of interfacial surfactant by exchange between the surface and bulk phase. Moreover, at high bulk concentration the interface is almost completely saturated with surfactant so that it cannot easily support a surface tension gradient. We find that the interface then ‘remobilizes’ in the sense that the tangential fluid velocity there approaches the surfactant-free velocity. The same effect has been shown to increase interfacial mobility and reduce drag for a steadily rising gas bubble in a fluid with a large concentration of bulk surfactant [45].

Our numerical method captures examples of tipstreaming drops, which, to the best of our knowledge, are the first resolved computations of tipstreaming with soluble surfactant. We characterize the dependence of the tipstreaming drop on physical parameters, and in particular show that the emitted filaments become thinner as the Biot number  $Bi$ , which is a ratio of the time scale for desorption to that for the flow, increases. An example of the tipstreaming of very thin threads in the widely-studied diffusion-controlled limit  $Bi \rightarrow \infty$  is given. We also present a phase diagram which gives operating conditions or parameter values for tipstreaming and compare with a similar diagram obtained from the microfluidics experiments of [3]. Despite the differences in geometry between the experiment and our computational set-up, we find general agreement in the parameter regime for tipstreaming.

The study is organized as follows. The problem formulation and governing equations

are given in §II, which includes a derivation of the reduced equations in the infinite Peclet number limit. The hybrid numerical method is presented in §III. Validation of the numerical method and the results of parameter studies are presented in §IV. Conclusions are given in §V. A scaling argument that elucidates immobilization and remobilization effects, and an asymptotic solution for small capillary number, which is used to verify the numerical method, are derived in an appendix §VI.

## II. GOVERNING EQUATIONS

We present the governing equations in dimensionless form. Consider an axisymmetric drop with viscosity  $\lambda\mu$  immersed in a fluid of viscosity  $\mu$  and stretched by an imposed extensional flow. The fluid inside the drop occupies a region  $\Omega_1$ , while the unbounded fluid exterior to the drop occupies the complementary region  $\Omega_2$ . The interface between the fluids is denoted by  $S$ . The two fluids are taken to have the same density, so that the drop is neutrally buoyant and gravitational effects are ignored. In the low Reynolds number limit, the bulk flow in each phase is governed by the incompressible Stokes equations

$$\lambda\nabla^2\mathbf{u}_1 = \nabla p_1, \quad \nabla \cdot \mathbf{u}_1 = 0, \quad \mathbf{x} \in \Omega_1, \quad (1)$$

$$\nabla^2\mathbf{u}_2 = \nabla p_2, \quad \nabla \cdot \mathbf{u}_2 = 0, \quad \mathbf{x} \in \Omega_2, \quad (2)$$

where  $\mathbf{u}_i = (u_{ir}, u_{ix})$  is the velocity and  $p_i$  is the pressure in region  $i$  in an axisymmetric cylindrical-polar coordinate system  $\mathbf{x} = r\mathbf{e}_r + x\mathbf{e}_x$ , where  $\mathbf{e}_r$  and  $\mathbf{e}_x$  are radial and axial unit vectors. All lengths are nondimensionalized by the radius  $R_0$  of the equivalent, undisturbed spherical drop. There is a choice for the velocity scale  $U$ , between either the imposed (extrinsic) velocity scale  $U = U_G = GR_0$ , where  $G$  is the strain rate, or the (intrinsic) capillary scale  $U = U_\gamma = \gamma_0/\mu_2$ . Here we choose  $U = U_G$ . Pressure and time are nondimensionalized by  $\mu U/R_0$  and  $R_0/U$ .

At the drop surface  $S$  the fluid velocity is continuous and we denote the common value by  $\mathbf{U}$ , that is

$$\mathbf{u}_1 = \mathbf{u}_2 = \mathbf{U} \quad \text{at } \mathbf{x} \in S. \quad (3)$$

The evolution of the interface shape is determined by the kinematic boundary condition

$$\frac{d\mathbf{x}}{dt} = (\mathbf{U} \cdot \mathbf{n})\mathbf{n}, \quad (4)$$

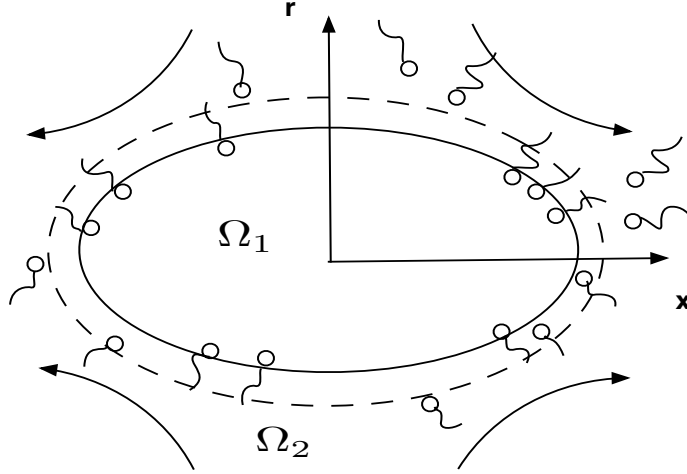


FIG. 1: A drop stretched by an imposed strain flow. Bulk soluble surfactant with concentration  $C$  is dissolved in the external phase.

which gives the motion of a point on the interface  $\mathbf{x}$  in the normal direction  $\mathbf{n}$ , here chosen to point outward from  $S$ . The difference in the fluid stress across  $S$  is equal to the net stress due to interfacial surface tension, which leads to the stress-balance boundary condition

$$-(p_2 - p_1)\mathbf{n} + 2(\mathbf{e}_2 - \lambda\mathbf{e}_1) \cdot \mathbf{n} = Ca^{-1}(\gamma\kappa\mathbf{n} - \nabla_s\gamma), \quad (5)$$

where  $\mathbf{e}_i$  is the rate-of-strain tensor in region  $\Omega_i$ ,  $\kappa = \kappa_\theta + \kappa_x$  is the sum of the principal normal curvatures of  $S$ ,  $\gamma$  is the surface tension made nondimensional by the surface tension of a clean or surfactant-free interface  $\gamma_0$ , and  $\nabla_s$  is the surface gradient  $\nabla_s = \nabla - \mathbf{n}(\mathbf{n} \cdot \nabla)$ . The parameter  $Ca = \mu_2 U / \gamma_0$  is the capillary number, which measures the ratio of viscous to surface tension forces.

This study focusses on the effect of soluble surfactant on the drop shape and dynamics. We nondimensionalize the bulk concentration of surfactant  $C$  by a uniform far-field value  $C_\infty$ , and the surface concentration  $\Gamma$  is nondimensionalized by the maximum monolayer packing concentration  $\Gamma_\infty$ . This surface saturation concentration  $\Gamma_\infty$  is a theoretical limit that can not be reached in practice due to constraints on the maximum bulk concentration such as the critical micelle concentration (CMC) [3], [11], [36]. The surfactant has bulk diffusion coefficient  $D$  and surface diffusion coefficient  $D_s$ , both of which are taken to be small. Surfactant can transfer or exchange between its adsorbed form on the interface and its dissolved form in the bulk immediately adjacent to the interface, with a desorption rate  $\kappa_d$  and adsorption rate  $\kappa_a$ .

The surface tension  $\gamma$  depends on the adsorbed concentration of surfactant  $\Gamma$  through an equation of state  $\gamma = \gamma(\Gamma)$ . The presence of surfactant at the interface generally reduces the surface tension, and a widely used surface equation of state is

$$\gamma = 1 + E \ln(1 - \Gamma), \quad (6)$$

where  $E = RT\Gamma_\infty/\gamma_0$  is the elasticity,  $R$  is the gas constant, and  $T$  is temperature. The elasticity parameter is a dimensionless measure of the sensitivity of surface tension to surfactant concentration. Equation 6 is described as the Frumkin surface equation of state [9] or a Langmuir-type surface equation of state [14].

For simplicity, surfactant is taken to be soluble only in the fluid region  $\Omega_2$ . Equations for the evolution of adsorbed and bulk surfactant are [14, 46]

$$\left. \frac{\partial \Gamma}{\partial t} \right|_n + \nabla_s \cdot (\Gamma \mathbf{u}_s) + \kappa u_n \Gamma = \frac{1}{Pe_s} \nabla_s^2 \Gamma + J \mathbf{n} \cdot \nabla C|_S, \quad \mathbf{x} \in S, \quad (7)$$

$$\left. \frac{\partial C}{\partial t} \right|_{\mathbf{x}} + \mathbf{u} \cdot \nabla C = \frac{1}{Pe} \nabla^2 C, \quad \mathbf{x} \in \Omega_2, \quad (8)$$

where  $\mathbf{u}_s$  is the tangential fluid velocity on  $S$ ,  $u_n$  is the normal component of fluid velocity of the interface,  $Pe_s = UR_0/D_s$  is the Péclet number for surface diffusion of adsorbed surfactant, and  $Pe = UR_0/D$  is the Péclet number for diffusion of bulk surfactant. The bulk and surface Peclet numbers are typically large in applications, and can be of the order of  $10^6$  or more. On the left hand side of equation (7), the first term represents the time derivative of  $\Gamma$  at a point on  $S$  that moves in the direction normal to the interface, which is referred to as a ‘fixed surface coordinate’ [46]. The next two terms account for the change in surfactant concentration due to advective flux along the interface and the change in local interfacial area caused by motion along the normal. The first term on the right hand side represents the change in  $\Gamma$  due to surface diffusion, which is usually neglected, while the second term accounts for the transfer or exchange of surfactant between its dissolved form in the bulk flow immediately adjacent to the interface and its adsorbed form on the interface (the subscript  $S$  denotes evaluation at the surface). The parameter  $J = C_\infty D/\Gamma_\infty U$  is a measure of transfer of surfactant between its bulk and adsorbed forms relative to advection on the interface. Note that  $J = 0$  corresponds to insoluble surfactant. The time derivative in the equation for  $C$  is at a fixed point  $\mathbf{x}$  in  $\Omega_2$ .

Exchange of surfactant between the bulk phase adjacent to the interface and the interface itself is a two-step process [14]. Surfactant in the bulk is transported by diffusion to the

‘sublayer’ or region near the interface, while exchange between the sublayer and the interface occurs via adsorption-desorption kinetics. The net rate of accumulation of surfactant on the interface is therefore equal to its rate of adsorption minus its rate of desorption and is also equal to the normal diffusive flux of bulk surfactant at the interface, so that

$$J\mathbf{n} \cdot \nabla C|_S = Bi(K(1 - \Gamma)C|_S - \Gamma), \quad \mathbf{x} \in S, \quad (9)$$

where  $K = \kappa_a C_\infty / \kappa_d$  is a dimensionless equilibrium partition coefficient representing the ratio of the adsorption rate  $\kappa_a$  to the desorption rate  $\kappa_d$ , and the Biot number  $Bi = R_0 \kappa_d / U$  is the ratio of the time scale  $R_0 / U$  of the flow to the time for desorption  $\kappa_d^{-1}$ .

The imposed far-field flow that stretches the drop is a pure axisymmetric strain flow, which has nondimensional form

$$\mathbf{u} \rightarrow \mathbf{u}^\infty = \left( -\frac{r}{2} \mathbf{e}_r + x \mathbf{e}_x \right), \quad \text{as } |\mathbf{x}| \rightarrow \infty. \quad (10)$$

The initial distribution of bulk surfactant is taken to be spatially uniform and its far-field value is constant in time, so that

$$C(\mathbf{x}, 0) = 1 \text{ for } \mathbf{x} \in \Omega_2, \quad C \rightarrow 1 \text{ as } |\mathbf{x}| \rightarrow \infty. \quad (11)$$

If the initial configuration is in equilibrium then the initial drop shape is spherical, and from (9) the initial surface concentration of surfactant is

$$\Gamma(\mathbf{x}, 0) = \Gamma_0 = K / (1 + K). \quad (12)$$

#### A. The limits $Bi \rightarrow \infty$ with $J$ fixed and $J \rightarrow \infty$ with $Bi$ fixed.

The limit of diffusion-controlled transport, in which  $Bi \rightarrow \infty$  with  $J$  fixed, is relevant in many applications. In this limit the adsorption-desorption surface exchange kinetics are in equilibrium, and the boundary condition (9) becomes

$$C|_S = \frac{\Gamma}{K(1 - \Gamma)}, \quad \mathbf{x} \in S. \quad (13)$$

This Dirichlet form of the interface boundary condition was considered in, for example, [7, 47].

Conversely, surfactant transport is adsorption-desorption or sorption-controlled when the rate of bulk diffusion is fast compared to the rate of surface exchange kinetics, that is,

when  $Bi/J = (\kappa_d R_0 \Gamma_\infty)/(DC_\infty) \ll 1$ . It was shown in [16] that this leads to a model for surfactant solubility dynamics which has been referred to as pseudo-solubility and is noted here. In an expansion with  $Bi/J$  as a small parameter, the boundary condition (9) implies that  $\partial_n C|_S = 0$  at leading order, and the governing equation (8), and initial and boundary conditions (11) then imply that  $C \equiv 1$ . The source or exchange term  $J\mathbf{n} \cdot \nabla C|_S$  in (7) is then given at the next order by the right hand side of (9) with  $C|_S = 1$ , so that equation (7) for the evolution of interfacial surfactant becomes

$$\left. \frac{\partial \Gamma}{\partial t} \right|_n + \nabla_s \cdot (\Gamma \mathbf{u}_s) + \kappa u_n \Gamma = \frac{1}{Pe_s} \nabla_s^2 \Gamma + Bi(K(1 - \Gamma) - \Gamma), \quad \mathbf{x} \in S. \quad (14)$$

Since the dependence on the bulk concentration no longer appears in the exchange term, the model has the same computational overhead as for insoluble surfactant, and it gives a consistent limit of solubility dynamics when  $Bi$  is fixed as  $J \rightarrow \infty$ . In exchange of surfactant between the interface and bulk phases, excess or depletion of bulk surfactant is removed or replenished instantaneously by fast bulk diffusion.

### B. Finite Biot number

Here we retain the more general interface boundary condition (9) to enable the study of drops at arbitrary values of the Biot number  $Bi$  and exchange parameter  $J$ . This is referred to as a ‘diffusion-kinetic’ or ‘mixed kinetic’ model [9], and its boundary condition is of mixed type. We also make the physically representative assumption that the strain rate  $G$  is much greater than the rate of bulk surfactant diffusion ( $D/R_0^2$ ), which implies that  $Pe \gg 1$ .

### C. The infinite bulk Peclet number limit

Equation (8) for  $C$  is singularly perturbed in the limit  $Pe \rightarrow \infty$ , and a narrow transition layer can develop near the interface in which the normal gradient of  $C$  is large. Away from this layer the leading order concentration remains uniform if it is uniform initially, which we assume here. We follow the approach taken in [7] where the leading order equation for the evolution of bulk surfactant in the transition layer is derived using matched asymptotic expansions. A brief derivation is given here for a general surface in a three-dimensional flow; further details can be found in [7].

An intrinsic or surface-fitted orthogonal coordinate system  $(\xi_1, \xi_2, n)$  is introduced that is attached to and moves with the surface  $S$  for all time. Here  $\xi_1$  and  $\xi_2$  are aligned with the principal directions of curvature and  $n$  is distance along the normal measured from  $S$ . The position vector  $\mathbf{x}$  of a point and the fluid velocity  $\mathbf{u}$  in a fixed Eulerian coordinate system is written as

$$\mathbf{x} = \mathbf{X}(\xi_1, \xi_2, t) + n\mathbf{n}(\xi_1, \xi_2, t), \quad (15)$$

$$\mathbf{u} = \mathbf{u}_t + u_p\mathbf{n}, \quad (16)$$

where  $\mathbf{x} = \mathbf{X}(\xi_1, \xi_2, t)$  is the equation of  $S$ , and  $\mathbf{u}$  is written in terms of its projection onto the tangent plane  $\mathbf{u}_t$  and its component in the normal direction  $u_p$ . We also define the fluid velocity  $\mathbf{v}$  relative to  $S$  as  $\mathbf{v} = \mathbf{v}_t + v_p\mathbf{n}$ . Here  $\mathbf{v}_t = \mathbf{u}_t - \mathbf{U}_s$  where  $\mathbf{U}_s = \mathbf{X}_t - \mathbf{X}_t \cdot \mathbf{n}$  is the tangential velocity of an interface point at fixed  $(\xi_1, \xi_2)$ , and  $v_p = u_p - u_n$  is the normal component of fluid velocity relative to  $S$ . As the interface is approached,  $\mathbf{u}_t$  approaches the tangential interfacial fluid velocity  $\mathbf{u}_s$  and  $v_p$  tends to zero.

In the large  $Pe$  limit,  $C$  can depend on a local normal coordinate  $N$  where  $n = \epsilon N$ ,  $\epsilon = Pe^{-1/2}$  is the order of the width of the transition layer, and  $N = O(1)$  as  $\epsilon \rightarrow 0$ . Although  $C = C(\xi_1, \xi_2, N, t; \epsilon)$  within the layer, there is no mechanism available to support a similar separation of scales for the fluid velocity, so that  $\mathbf{v} = \mathbf{v}_t + v_p\mathbf{n} = \mathbf{v}(\xi_1, \xi_2, n, t; \epsilon)$ . An equation for the evolution of  $C$  within the layer that is exact in the limit  $Pe \rightarrow \infty$  is given by keeping only the leading terms in an expansion for small  $\epsilon$ . This reduced equation is

$$\left. \frac{\partial C}{\partial t} \right|_{\xi_1, \xi_2} + \mathbf{v}_s \cdot \nabla_s C + \left. \frac{\partial v_p}{\partial n} \right|_S N \frac{\partial C}{\partial N} = \frac{\partial^2 C}{\partial N^2}, \quad \mathbf{x} \in \Omega^r \quad (17)$$

where  $\mathbf{v}_s = \mathbf{u}_s - \mathbf{U}_s$  is the tangential interfacial fluid velocity relative to an interface point with fixed  $(\xi_1, \xi_2)$  and  $\Omega^r$  is the transition layer subdomain of  $\Omega_2$ . Consideration of higher order terms in the expansion implies that the error in approximating  $C$  by the solution of this equation is of order  $O(\epsilon)$  as  $\epsilon \rightarrow 0$ .

The large  $Pe$  limit implies that outside the transition layer  $(\partial_t + \mathbf{u} \cdot \nabla)C = 0$  to within  $O(\epsilon)$ , so that  $C$  is constant on particle paths to the same order. The initial condition of (11), that  $C(\mathbf{x}, 0) = 1$  everywhere, implies that  $C \equiv 1$  outside the transition layer for all time and provides initial and matching conditions

$$C(\xi_1, \xi_2, N, 0) = 1, \quad C(\xi_1, \xi_2, N, t) \rightarrow 1 \quad \text{as } N \rightarrow \infty \quad \text{for } t > 0. \quad (18)$$

The transfer coefficient  $J$  in the bulk-interface surfactant exchange term  $J\partial_n C|_S$  is rescaled by putting  $J = \epsilon J_0$  where  $J_0 = O(1)$ , so that the exchange term remains  $O(1)$  when expressed in terms of the rescaled coordinate  $N$ . The mixed boundary condition (9) then becomes

$$J_0 \frac{\partial C}{\partial N} = Bi (K(1 - \Gamma)C|_S - \Gamma) \quad \text{at } N = 0, \quad (19)$$

while the boundary condition when  $Bi = \infty$  at (13) remains unchanged.

The coefficient  $\partial_n v_p|_S$  in equation (17)) appears to require evaluation of off-surface data to compute the normal derivative. However, the incompressibility condition  $\nabla \cdot \mathbf{u} = 0$  written in the intrinsic frame provides an expression for this coefficient in terms of surface data alone

$$\left. \frac{\partial v_p}{\partial n} \right|_S = -\kappa u_n - \nabla_s \cdot \mathbf{u}_s. \quad (20)$$

The bulk-interface surfactant exchange term in equation (7) is similarly rescaled, so that this equation becomes

$$\left. \frac{\partial \Gamma}{\partial t} \right|_n + \nabla_s \cdot (\Gamma \mathbf{u}_s) + \kappa u_n \Gamma = \frac{1}{Pe_s} \nabla_s^2 \Gamma + J_0 \frac{\partial C}{\partial N} \quad \text{at } N = 0. \quad (21)$$

Note that the expansion parameter  $Pe$  does not appear in the initial boundary value problem (17)–(21) for  $C$  and  $\Gamma$ . This is a consequence of the singular perturbation expansion retaining only leading order quantities in the limit  $Pe \rightarrow \infty$ . The surface and bulk Peclet numbers are often of the same order of magnitude, but unlike the treatment of bulk diffusion, the surface diffusion term  $Pe_s^{-1} \nabla_s^2 \Gamma$  has sufficiently small influence that it is often neglected [47].

An equation representing conservation of the total amount of surfactant is obtained by integrating (21) over the drop surface. The integral of the left hand side is equal to the time rate of change of the total amount of surfactant,  $\frac{d}{dt} \int_S \Gamma dS$  [38], so that

$$\frac{d}{dt} \int_S \Gamma dS = J_0 \int_S \frac{\partial C}{\partial N} dS = J_0 \text{Nu}, \quad (22)$$

where Nu is a Nusselt number [31]. This equation is used to check or validate our numerical method by verifying that the integral on the right hand side approaches zero as the evolution nears a steady state. For insoluble surfactant  $J_0 \partial_N C = 0$ , and the interfacial surfactant is conserved.

The diffusion-controlled and sorption-controlled limits of the boundary condition (19) can be recovered from the current  $Pe \rightarrow \infty$  formulation. The diffusion-controlled limit is found when  $Bi \rightarrow \infty$  with  $J_0$  fixed, for which the interface boundary condition is again

(13). The sorption-controlled limit is found when  $J_0 \rightarrow \infty$  with  $Bi$  fixed, and leads to the same pseudo-solubility model of equation (14). In this study we take  $Bi$  and  $J_0$  to be arbitrary and  $O(1)$  as  $Pe \rightarrow \infty$ , and the computational overhead relative to study of insoluble surfactant requires off-surface evaluation of  $C$  alone within the transition layer, since the fluid advection terms of (17) require only on-surface data.

### III. HYBRID NUMERICAL METHOD

Numerical methods based on a boundary integral representation, or boundary integral methods, have the advantage that they can be of arbitrarily high-order accuracy. Thus, they are useful for investigating phenomena that require high accuracy to resolve features, such as ‘pinching’ or topological singularities that can occur on the interface [26]. When the flow is axisymmetric, the surface integrals can be reduced to line integrals by performing the azimuthal integration analytically and evaluating the resulting elliptic integrals by recursive formulae [32]. The velocity at a point  $\mathbf{x}_0$  on the axisymmetric drop interface is governed by the boundary integral equation

$$\begin{aligned} u_\alpha(\mathbf{x}_0) + \frac{\lambda - 1}{4\pi(\lambda + 1)} \int_I^{PV} Q_{\alpha\beta\gamma}(\mathbf{x}, \mathbf{x}_0) u_\beta(\mathbf{x}) n_\gamma(\mathbf{x}) ds(\mathbf{x}) \\ = \frac{2}{1 + \lambda} \mathbf{u}_\alpha^\infty(\mathbf{x}_0) + \frac{1}{4\pi(\lambda + 1)} \int_I M_{\alpha\beta}(\mathbf{x}, \mathbf{x}_0) (\nabla_s \gamma - \gamma \kappa \mathbf{n})_\beta(\mathbf{x}) ds(\mathbf{x}), \end{aligned} \quad (23)$$

see, for example, [2], [32], [37] and [38]. Here the subscripts  $\alpha, \beta, \gamma$  are either  $r$  or  $x$ , the radial and axial coordinates, and the boundary curve  $I$  traces the contour of the surface  $S$  in the  $(r, x)$  meridional plane. The curve is parameterized as

$$\mathbf{x} = \mathbf{X}(\xi, t) = r_s(\xi, t) \mathbf{e}_r + x_s(\xi, t) \mathbf{e}_x \quad (24)$$

and has differential arclength  $ds = [(\partial_\xi r_s)^2 + (\partial_\xi x_s)^2]^{1/2} d\xi$ , outward normal  $\mathbf{n}$  and curvature  $\kappa = \kappa_\theta + \kappa_x$ . The kernels  $Q_{\alpha\beta\gamma}$  and  $M_{\alpha\beta}$  are the axisymmetric version of the Stresslet distribution (or double layer potential) and the Stokeslet distribution (or single layer potential) respectively. The superscript  $PV$  denotes the principal value. Equation (23) is a second-kind Fredholm integral equation for  $\mathbf{u}(\mathbf{x}_0)$  except when the drop viscosity matches the exterior fluid viscosity or  $\lambda = 1$ , in which case the velocity is determined by a simpler single layer potential alone. In addition to axisymmetry, the interface is symmetric about

the plane  $x = 0$ , and the numerical method evolves only its trace in the first quadrant  $x \geq 0, y \geq 0$ .

The curve  $I$  is approximated by a set of boundary nodes along the contour in the  $(r, x)$  meridional plane. Following Stone and Leal [37] we discretize (23) assuming the fluid velocity varies linearly over each boundary element. Integrals with nonsingular kernels are computed by standard 8- or 16-point Gauss-Legendre quadrature, with the interface position at the quadrature points obtained by cubic spline interpolation from the positions of the nodes. The diagonal components  $M_{rr}, M_{zz}$  of the single-layer potential in (23) exhibit logarithmic singularities as  $\mathbf{x} \rightarrow \mathbf{x}_0$ , and the corresponding weakly singular integrals are calculated accurately using Gauss-log quadrature [44]. When  $\lambda = 0$  there is a zero eigenvalue or degeneracy of the integral equation (23), and we use a method of Pozrikidis [32] to remove the associated eigenfunction. Derivatives of  $\mathbf{X}(\xi, t)$  and the interface curvature are calculated using cubic-splines, which are also used to implement an adaptive grid technique similar to that of [26], whereby grid points are redistributed locally so that their spacing in arclength is inversely proportional to the interface curvature. This adaptive technique effectively resolves high curvature regions such as the drop tips or a necking region before pinch-off.

The linear system formed by discretization of the integral equations is solved by a LAPACK Gaussian elimination routine. Once the interfacial velocity is known, the marker points are advanced by local normal velocities according to the kinematic boundary condition (4), implying that the parameter  $\xi$  is a fixed surface coordinate during the time step. We use a first-order forward Euler method for the time update of the interface node points. In a typical computation, the interface profile is represented by about 160-240 points over the first quarter the drop.

### 1. Mesh-based method for the transition layer

The transition layer is defined on a fixed rectangular domain in  $(\xi, N)$  coordinate space, where the advection-diffusion equation (17) holds. The problem for  $C(\xi, N, t)$  is

$$\frac{\partial C}{\partial t} \Big|_{\xi} + \frac{v_s(\xi, t)}{l(\xi, t)} \frac{\partial C}{\partial \xi} + \psi(\xi, t) N \frac{\partial C}{\partial N} = \frac{\partial^2 C}{\partial N^2}, \quad (25)$$

where  $v_s = u_s - U_s$  and  $\psi(\xi, t) = - \left( \kappa u_n + \frac{1}{l} \frac{\partial u_s}{\partial \xi} \right)$

with initial and boundary conditions (18) and (19). Here  $l(\xi, t) = |\partial_\xi \mathbf{x}(\xi, t)|$ ,  $u_n$  and  $u_s$  are the normal and tangential components of the interfacial fluid velocity  $\mathbf{u}$ , and  $U_s$  is the tangential component of  $\mathbf{U}_s$ . The specification of  $\xi$  as a fixed surface coordinate implies that  $U_s = 0$  [46].

The mesh-based method for the transition layer is second order accurate in space and uses an explicit, first order Euler method for the time update, although in principle it can be made higher-order accurate (a spectrally accurate implementation in space in 2D is given in [47]). Equispaced collocation points  $N_j = j N_M/M$ ,  $j = 0, \dots, M$ , are introduced in the normal  $N$  direction, where  $N = N_M$  is a finite artificial boundary. Equation (25) is discretized using second order finite differences in space, with nonuniform difference formulae used in the tangential  $\xi$ -coordinate, since points become unevenly spaced during the adaptive grid procedure. Boundary condition (19), or (13) when  $Bi = \infty$ , is applied at the drop surface. We also need the first and second normal derivatives of the bulk surfactant concentration evaluated at the drop surface, which are calculated using second order, one-sided difference formulas.

At the artificial far-field boundary  $N = N_M$  our earlier studies [7, 47] imposed the matching condition  $C = 1$  of (18). Here, we implement an improved version of the boundary condition that better resolves the structure of the transition layer near stagnation points on the bubble surface at which the flow direction is away from the interface. This is of interest when, for example, the capillary number of the imposed flow is sufficiently small that the drop attains a steady shape but surfactant that is advected to the drop end stagnation points has sufficient time to accumulate and reach high concentration, eventually forming a plume of surfactant that leaves the transition layer, see Figure 4 of [7] which shows such a structure beginning to form. The improved condition at the boundary  $N = N_M$  is

$$C(\xi_j, N_M) = 1 \text{ when } \frac{\partial v_p}{\partial n}(\xi_j, t) < 0, \quad (26)$$

$$C(\xi_j, N_M) \text{ is 'free' (i.e., determined from (25)) when } \frac{\partial v_p}{\partial n}(\xi_j, t) \geq 0, \quad (27)$$

where  $\partial v_p / \partial n$  is computed using (20). The first relation enforces the matching condition (18) at points on the boundary  $N = N_M$  where the characteristic or advective flow is inward, into the transition layer, while the second condition allows the bulk surfactant to advect correctly out of the computational domain  $\Omega'$  when the local flow is directed away from the layer. The second condition (27) is imposed using one-sided derivatives in  $N$  for the

discretization of (25) at the far-field boundary. We solve equation (21) simultaneously for the interfacial concentration of surfactant  $\Gamma$ , which is discretized as in [38].

In the presentation of results we follow [16] and redefine the velocity scale to be  $U = U_\gamma = \gamma_0/\mu_2$ . Any dimensionless group, such as  $Bi = \kappa_d R_0/U$ , that depends on  $U$  is given a prime to denote its rescaled value with the choice  $U = U_\gamma$  and is related to its value with the choice  $U = U_G = GR_0$  by the ratio, which is the capillary number  $Ca = GR_0\mu_2/\gamma_0$ . So

$$Pe' = Pe Ca^{-1}, \quad Pe'_s = Pe_s Ca^{-1}, \quad Bi' = Bi Ca, \quad J' = J Ca, \quad \text{and} \quad J'_0 = J_0 Ca^{1/2}. \quad (28)$$

The groups with primes are fixed by the intrinsic properties of the fluids and surfactant, and are independent of the strain rate, which then only appears in  $Ca$ . Since the choice of velocity scale also appears in the nondimensionalization, some of the dimensionless variables are also rescaled, namely,

$$\mathbf{u}' = \mathbf{u} Ca, \quad t' = t Ca^{-1}, \quad p' = p Ca, \quad \text{and} \quad N' = N Ca^{-1/2}.$$

In terms of the rescaled quantities,  $Ca$  no longer appears in the stress-balance boundary condition (5) and appears only in the imposed flow

$$\mathbf{u}' \rightarrow \mathbf{u}'^\infty = Ca \left( -\frac{r}{2} \mathbf{e}_r + x \mathbf{e}_x \right), \quad \text{as } |\mathbf{x}| \rightarrow \infty.$$

An example numerical calculation is shown in Figure 2 for the parameter values  $\lambda = 1$ ,  $E = 0.15$ ,  $Bi' = 0.1$ ,  $K = 0.5$ ,  $J'_0 = 0.05$ , and  $Ca = 0.04$ . Here and in all subsequent examples, the interface is initially spherical and the surface and bulk surfactant concentration are in equilibrium so that  $\Gamma_0 = K/(1+K)$ , per equation (12). Also, the surface Peclet number is  $Pe'_s = 10^3$  throughout. At this small capillary number a steady, slightly deformed shape is reached at  $t \simeq 80$  as shown by the plot of maximum normal velocity in the top panel of Figure 2(a) and the surface profile in Figure 2(b). However, the bulk and surface surfactant concentration evolve more slowly, approaching a steady state after  $t \simeq 300$ . At steady state, the amount of surfactant adsorbed onto the interface at the equator of the drop ( $x \simeq 0$ ) is balanced by the amount desorbed at the poles or tips, per the conservation equation (22). The numerical method accurately captures this conservation, as indicated by the Nusselt number tending to zero in the second panel of Figure 2(a). The bulk concentration  $C$  at times  $t = 75$ , 189, and 471 is shown in Figure 2(b). The boundary condition (27) prevents surfactant from being trapped at the far-field boundary near the drop tips, and allows it to advect out of the computational domain and form a high-concentration wake or plume.

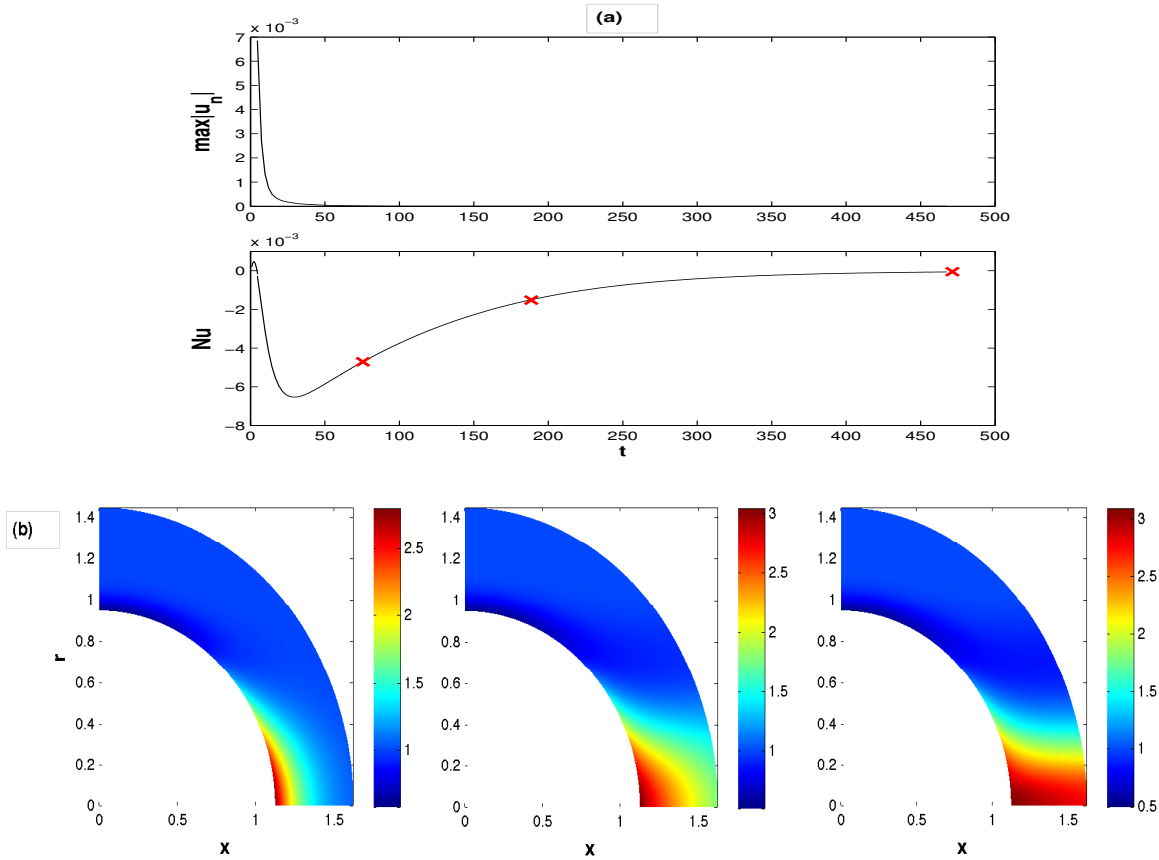


FIG. 2: (a) Evolution of  $\max(|u_n|)$  and Nusselt number  $Nu$  versus  $t$ . (b) Bulk concentration  $C$  at times  $t = 75, 189, 471$ , which are marked by crosses in Fig. 2(a). The Peclet number is set to  $Pe = 10^4$  to depict the bulk concentration  $C$  in the layer.

## IV. NUMERICAL RESULTS AND DISCUSSION

### A. Validation

When the surfactant is insoluble the method has been validated by comparison with solutions presented in [38], [33], and [17]. In particular, we have reproduced Figure 3 of [38], which compares numerical results to an asymptotic solution for small capillary number. The total surfactant mass is conserved to within about 1% in a typical computation, and the volume is conserved to within 0.001%.

The implementation of the hybrid method with soluble surfactant ( $J'_0 > 0$ ) was checked to have the expected accuracy, being second order in space and first order in time, and was further verified by comparison with analytical solutions. An analytical solution given in [45]

describes the unsteady adsorption of surfactant from a spatially uniform bulk state  $C = 1$  on to an initially clean spherical drop surface in the absence of flow when the surface is an infinite sink of surfactant, i.e.  $C|_S = 0$  for all  $t$ . Our computations give excellent agreement with this analytical solution.

We also compare with an asymptotic solution of the transition layer and fluid equations that is valid for small capillary number  $Ca \ll 1$  when  $E = 0$ , which is derived in the appendix §VI. This solution describes the steady state shape and bulk surfactant concentration for a drop in an imposed strain when the surface is an infinite sink of surfactant (i.e.,  $C|_S = 0$ ). A similar test was made for 2D flow in [7]. To leading order, the steady surface velocity is given by (35) and we find a similarity solution  $C = \text{erf}(\eta)$  of the transition layer equation, where  $\eta = c_0 N/g(\phi)$ ,  $c_0$  is a constant and  $g(\phi)$  is a function of the angle of declination from the positive  $x$  axis. Figure 3 compares the asymptotic solution with a solution computed by the hybrid numerical method when  $Ca = 0.015$  and the viscosity ratio  $\lambda = 1$ . The figure shows the bulk surfactant concentration  $C(N, \phi)$  versus the normal coordinate  $N$  at positions  $\phi_i$  that are equidistant along the drop surface in the first quadrant of the  $x$ - $y$  plane. The dashed lines denote the numerical results of the hybrid method, which was run until the solution reaches a steady state ( $t \simeq 400$ ), and the symbols give the asymptotic solution (37). The lowest curve corresponds to  $\phi = 0$  at the drop tip and the curves rise with increasing  $\phi$  to  $\phi = \pi/2$  at the drop equator. Similar agreement is obtained for other values of  $\lambda$  (not shown).

### B. Steady deformation for $\lambda = 0$ and $Bi' = \infty$

A canonical problem is that of an inviscid bubble ( $\lambda = 0$ ) stretched by an imposed strain flow. For a clean or surfactant-free bubble, slender body theory [8] and numerical computations [1] provide strong evidence that a steady-state solution exists for all values of the capillary number  $Ca$ . Furthermore, the steady solutions are believed to be stable and attracting, and this has been verified over the finite range of capillary numbers ( $0 \leq Ca \lesssim 1$ ) that has been studied by time-dependent numerical computations (see, e.g., [15]). In contrast, when the bubble is coated with insoluble surfactant, asymptotic theory [6] and numerical computations [38] suggest that there is a critical capillary number  $Ca_c$  above which a steady solution no longer exists. For  $Ca > Ca_c$  the bubble lengthens in time without limit,

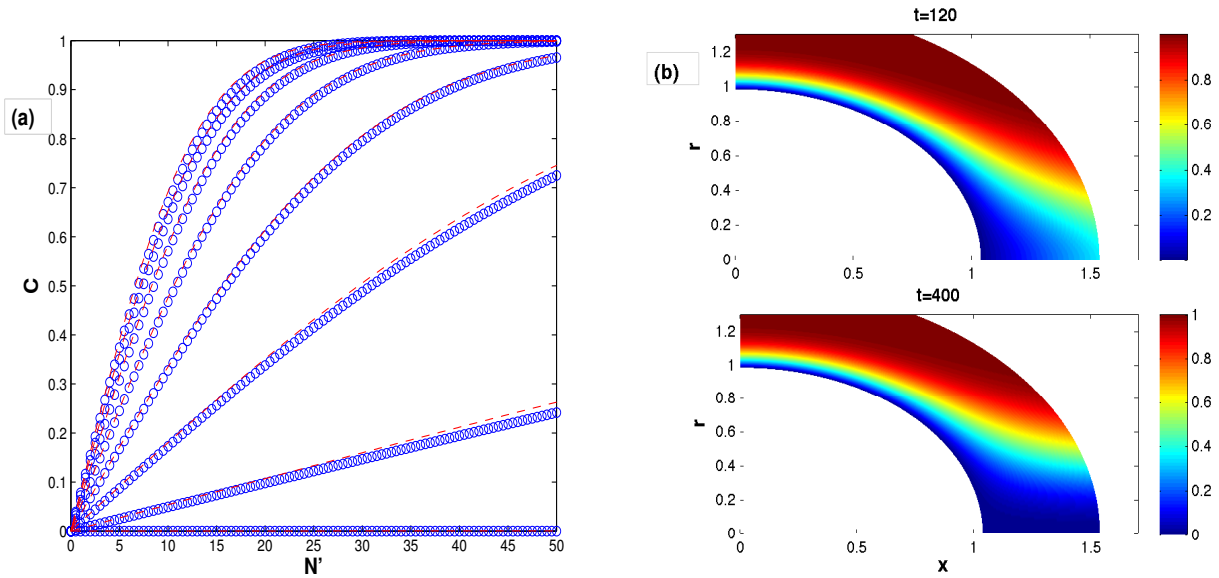


FIG. 3: (a) Comparison between the steady-state asymptotic solution (37) (symbols) and the solution computed by the hybrid method (dashed lines) when  $Ca = 0.015$ ,  $\lambda = 1$  and  $t \gg 1$ , showing the bulk concentration  $C(N, \phi_i)$  for different  $\phi_i$ . (b) The bulk concentration at times  $t = 120$  and  $400$  with  $Pe = 10^4$ .

or ‘bursts’ [6] [17]. In sections IV B 1 – IV B 3 the effect of surfactant solubility on steady solution branches for an inviscid bubble is investigated. We first consider the diffusion controlled regime, i.e. the limit  $Bi' \rightarrow \infty$ , in which surfactant exchange kinetics are in equilibrium and the surface boundary condition is (13).

### 1. Varying $J'_0$ with $K$ fixed

Change in  $J'_0$  with  $K$  fixed corresponds to changing the dimensional surfactant concentration at infinity,  $C_\infty$ , together with the ratio of adsorption to desorption rates so that  $K = \kappa_a C_\infty / \kappa_d$  and all other parameters remain fixed. Since the normal derivative of the bulk surfactant concentration at the bubble surface  $\partial C / \partial N'$  stays bounded, in the limit  $J'_0 \rightarrow 0$  equations (13), (17), and (18) become uncoupled from equation (21) and the remainder of the system, so that the dynamics of an insoluble surfactant is recovered.

Figure 4 examines the influence of surfactant solubility via change in  $J'_0$  on steady solution branches at  $E = 0.2$ ,  $K = 0.5$ , and  $\Gamma_0 = 1/3$  per (12)). The figure plots the bubble shape

as measured by the Taylor deformation number

$$D = \frac{|L - B|}{L + B} \quad (29)$$

versus  $Ca$ , where  $L$  and  $B$  are the bubble half-lengths in the  $x$  and  $r$  directions, respectively. The branches are computed by using the hybrid numerical method to time-evolve the interface to a steady-state shape at some value of  $Ca$ , followed by a continuation procedure where this solution is used as initial data for computation at slightly larger  $Ca$ . The solution branches are terminated when the bubble tips have sufficiently high curvature that they are difficult to resolve ( $\kappa \simeq 100$ ), or when the solution becomes unsteady.

The solid curve at the far right of Figure 4 shows our computation of the clean-bubble solution branch. This is close to the asymptotic small  $Ca$  deformation analysis of [4], which is denoted by a dashed line, as well as the computational results of [15], [49], which are not shown. The bubble shapes on this curve are smooth but for sufficiently large  $Ca$  become ‘pointed’, with large curvature at the tips. The pointed bubble shapes are similar to those obtained by slender body theory and steady-state numerical computations [8], [49], [15]. The dot-dash curve at the far left in the figure is the solution branch for a bubble coated with insoluble surfactant,  $J'_0 = 0$ . This curve terminates in an approximately ellipsoidal-shaped bubble with a rounded tip [6] at a critical capillary number  $Ca_c \approx 0.1$ , and for larger  $Ca$  we observe only unsteady (tipstreaming) solutions, which develop large curvature at the tips. Slender body theory [6] suggests the existence of a turning point in this solution branch which connects to an upper branch of unstable steady states. We conclude that the turning point defines a critical capillary number  $Ca_c$ , above which there are no steady solutions.

Surfactant solubility ( $J'_0 > 0$ ) gives a mechanism that bridges from the behavior observed for insoluble surfactant to that of a clean bubble. For the relatively small value  $J'_0 = 0.003$ , surfactant exchange is weak and the solution branch is near that for insoluble surfactant. As  $J'_0$  increases, the steady solution branch tends toward that for the clean case. This is due to enhanced surfactant exchange between the interface and bulk fluid, since interfacial surfactant that is swept to the bubble tips by the imposed flow is more easily desorbed, as seen in the solution branches of Figure 4. A consequence of this is that the interfacial surfactant gradient and Marangoni force at the bubble tips is reduced, and the slip velocity at the interface is greater than it would be with insoluble or slightly soluble surfactant. This is a form of interface ‘remobilization’, similar to that of [45], and tends to promote dynamics

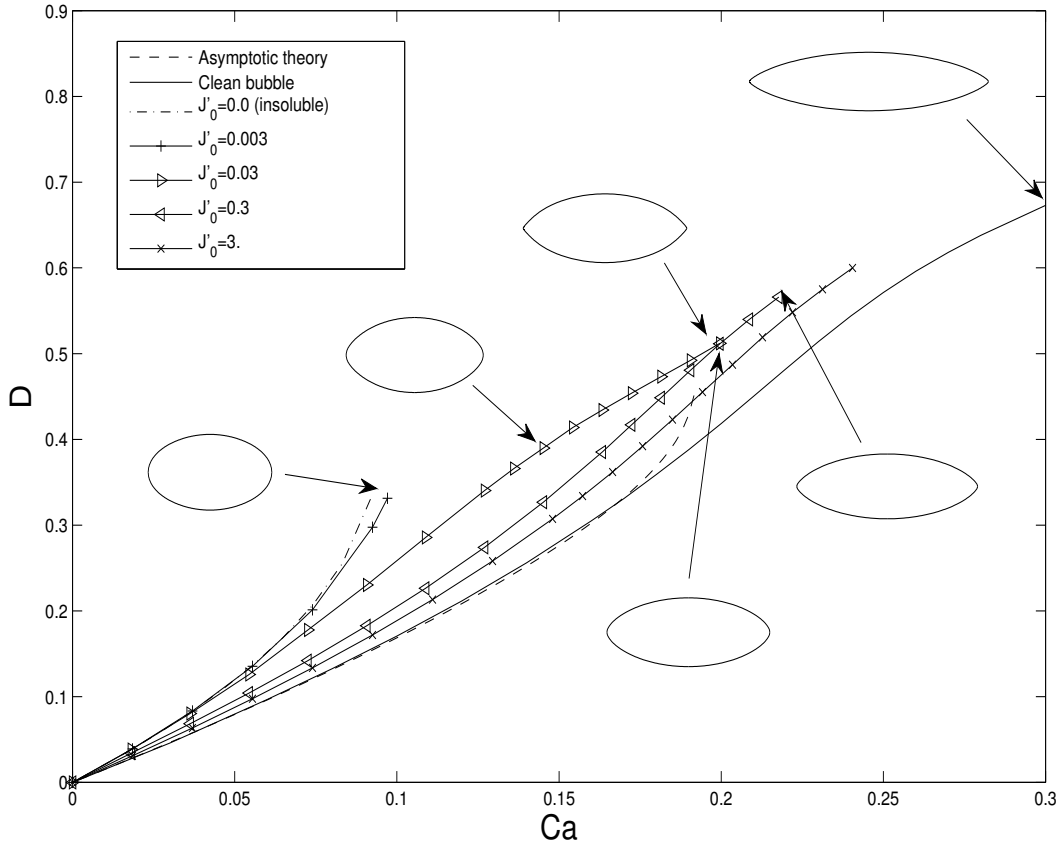


FIG. 4: Steady-state response curves for a bubble in an axisymmetric extensional flow as surfactant exchange parameter  $J'_0$  is varied ( $Bi' = \infty$ ). The dashed curve is the asymptotic result for a clean bubble of [4]. For other parameter values, see text.

that are surfactant-free or ‘clean’. In particular, remobilization can hinder bubble burst or tipstreaming by requiring a higher capillary number for its occurrence, or can eliminate it completely.

This surface remobilization is quantified in Figure 5(a), which plots the tangential component of surface velocity  $u_s$  versus a normalized arclength  $s^*$  at a fixed capillary number  $Ca = 0.06$  for different  $J'_0$ . The corresponding interfacial surfactant concentration  $\Gamma$  is given in Figure 5(b). For  $J'_0$  small, e.g.  $J'_0 \lesssim 10^{-2}$ ,  $\Gamma$  and  $u_s$  are close to that of the insoluble limit, and there is a relatively large Marangoni stress  $|\nabla_s \gamma|$  that acts in the opposite direction of the applied strain, see Figure 5(c). At larger  $J'_0$ ,  $J'_0 \gtrsim 10^{-1}$ , enhanced surfactant mass transfer between the interface and the bulk leads to surface remobilization, as seen in the surface velocity  $u_s$  at  $J'_0 = 0.3$ , which is near its surfactant-free value, and there is a more

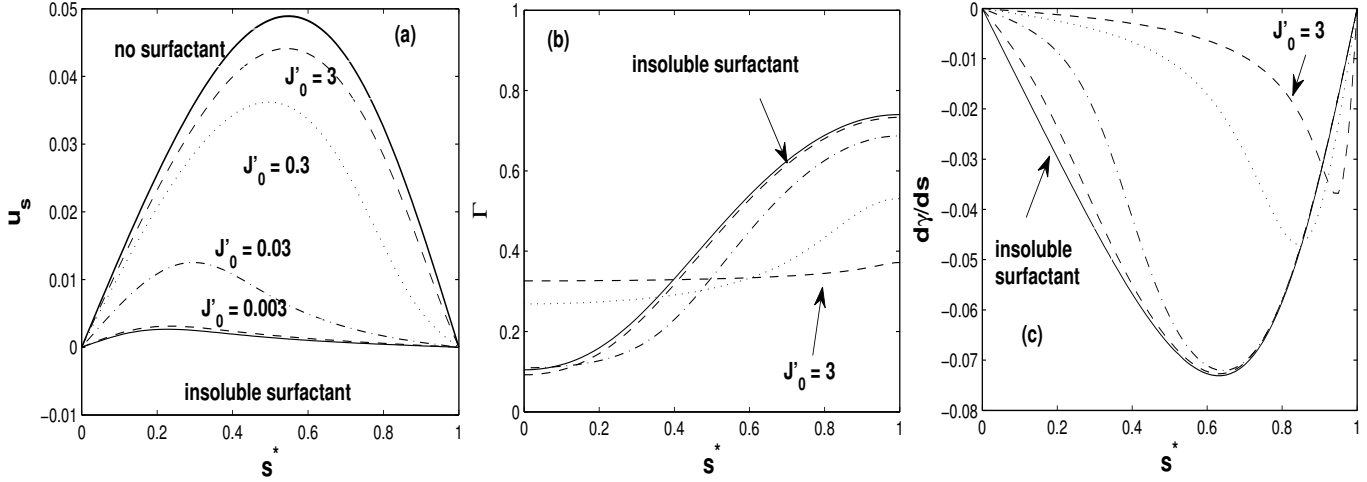


FIG. 5: (a) Tangential surface velocity  $u_s$  versus normalized arclength  $s^*$ ,  $s^* = 0$  at the drop equator and  $s^* = 1$  at the tip, for different  $J'_0$  at fixed capillary number  $Ca = 0.06$ . The upper solid curve is for a surfactant-free drop, and the lower solid curve is for insoluble surfactant. (b) Interfacial surfactant concentration  $\Gamma$ . (c) Marangoni stress  $d\gamma/ds$ . Other parameters as in Fig. 4.

uniform interfacial surfactant concentration and reduced Marangoni stress. The reduced Marangoni stress is less effective at destabilizing the steady bubble solution, and the onset of bursting or tipstreaming occurs at higher capillary number compared with the behavior at lower  $J'_0$ .

## 2. Varying $K$ , with $J'_0$ fixed

For a spherical drop in equilibrium with no flow, our choice of nondimensional variables implies that  $C = 1$  everywhere, and in particular  $C|_s = 1$ . The equilibrium value of adsorbed surfactant  $\Gamma_0$  is given by (12), which shows that at a large rate of adsorption relative to desorption, that is at large  $K$ , the equilibrium value of  $\Gamma_0$  is also large, i.e. close to the maximum packing density. Conversely, at small  $K$  surfactant desorbs more readily and the equilibrium value of  $\Gamma_0$  is small. In this way the limits of large and small  $K$  correspond to surfactant that is only slightly soluble in the bulk flow and to surfactant that is highly soluble, respectively. In the latter case the interface evolves as though it is more nearly surfactant-free.

Figures 6 and 7 show the influence of surfactant solubility on steady-state solution

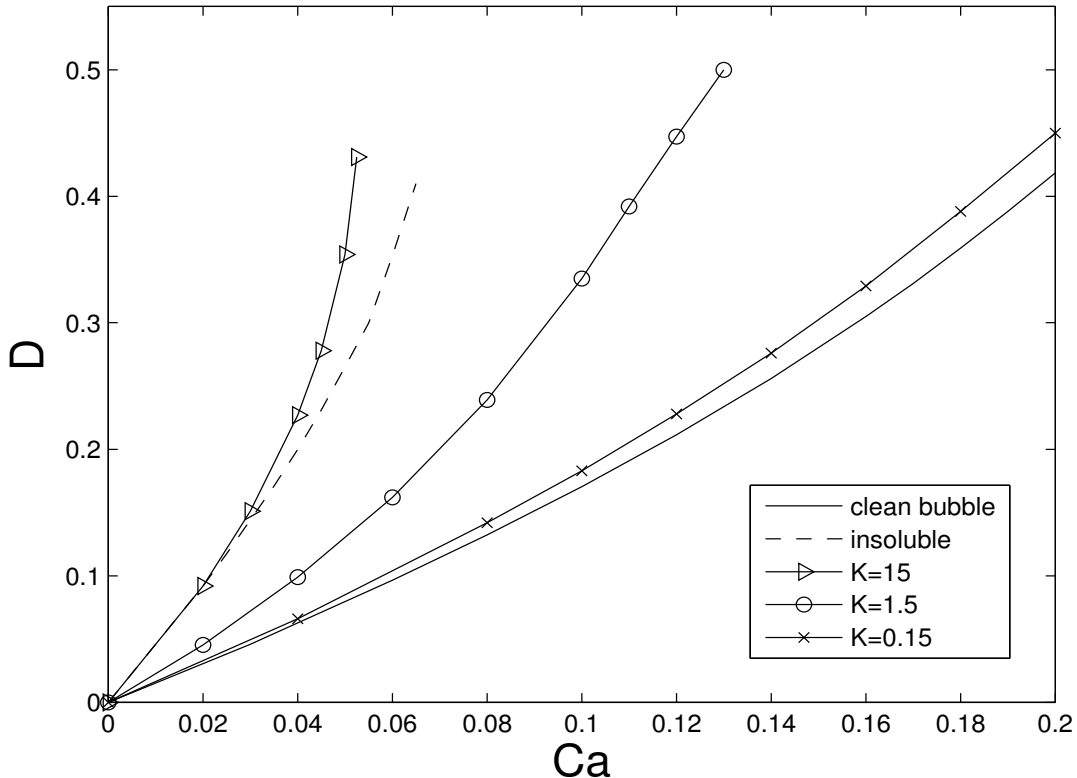


FIG. 6: Steady-state response showing deformation  $D$  versus capillary number  $Ca$  for a bubble in an axisymmetric extensional flow at different values of the equilibrium partition coefficient  $K$ . The response curve for a bubble coated with insoluble surfactant, given by a dashed curve, has the same initial surface concentration for soluble surfactant when  $K = 15$ . Other (fixed) parameter values are given in the text.

branches by varying  $K$  with  $\Gamma_0 = K/(1 + K)$  and other parameters fixed at  $\lambda = 0$ ,  $E = 0.2$ ,  $Bi' = \infty$ , and  $J'_0 = 0.1$ . For  $K$  small, the surfactant is highly soluble so that significant accumulation of interfacial surfactant and development of Marangoni stress does not easily occur. We therefore expect the steady-state deformation to be similar to that for a surfactant-free or clean interface, and this is seen in Figure 6, where the solution branch for the relatively small value of  $K = 0.15$  is near that for a clean bubble. Similarly, Figure 7, for which the data is given at fixed  $Ca = 0.04$ , shows the tangential surface velocity  $u_s$  versus  $s^*$  in part (a), and for  $K = 0.15$  this is close to the result for the clean case. Conversely, for large  $K$ , the rate of desorption is slow relative to adsorption so that large surface concentrations and

large Marangoni stress can develop. The surface is immobilized, in that the tangential interface velocity is reduced, and is similar to that for a drop coated with insoluble surfactant. We see from Figure 7(b) that even for the moderate value  $K = 1.5$ , both the interfacial velocity  $u_s$  is significantly reduced, and the steady deformation branch of Figure 6 is skewed toward the branch of the insoluble limit. At larger  $K = 15$  the solution branch and interfacial velocity are increasingly close to the insoluble limit. Figure 7(c) shows that significant Marangoni stress develops and the surface is almost completely immobilized. This suggests that increasing  $K$  with other parameters held fixed can promote tipstreaming and bubble burst.

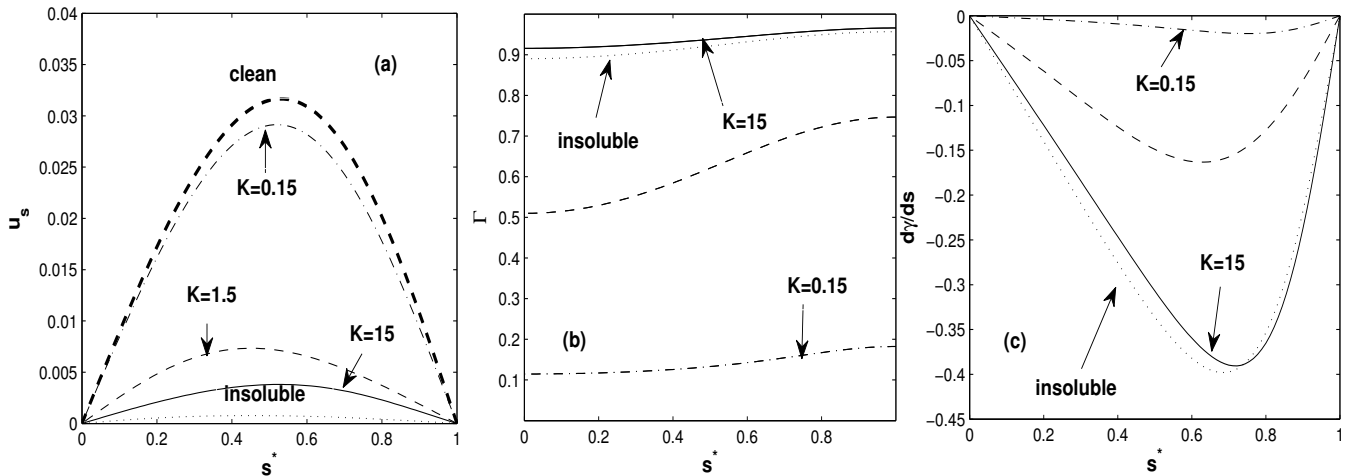


FIG. 7: (a) The tangential surface velocity  $u_s$  and (b) interfacial surfactant concentration  $\Gamma$  versus normalized arclength  $s^*$ , for various  $K$ . (c) Marangoni stress  $d\gamma/ds$  versus  $s^*$ . Other (fixed) parameter values are as in Figure 6

We note that in Figure 6, for insoluble surfactant the initial concentration  $\Gamma_0$  is chosen to be the same as that for a bubble with soluble surfactant when  $K = 15$ , i.e.,  $\Gamma_0 = 15/16$ . In both cases the interface is almost immobilized, but perhaps surprisingly, the steady deformation of the bubble with soluble surfactant is greater than that with insoluble surfactant at the same capillary number. This occurs because the influence of solubility at this large value of  $K$  is for the total surfactant concentration on the bubble surface  $\int \Gamma dS$  to increase above its initial value as  $t \rightarrow \infty$ . This causes a lower surface tension at the bubble tips compared to the insoluble surfactant case, and leads to greater stretch or deformation.

### 3. Varying $C_\infty$ .

Both the transfer coefficient  $J'_0$  and the partition coefficient  $K$  are directly proportional to the ambient bulk surfactant concentration  $C_\infty$  so that change in  $C_\infty$  with other parameters fixed corresponds to change in  $J'_0$  and  $K$  with  $J'_0/K$  fixed. When a bubble is stretched in an imposed strain flow, an increase in  $C_\infty$  enhances surfactant adsorption onto the surface at the bubble equator, from which it is advected by the imposed flow to the endpoints, where it accumulates and may desorb. This increase initially raises the magnitude of the surfactant concentration gradient and Marangoni stress on the interface, which reduces the surface velocity and promotes bubble deformation and breakup. Figure 8 shows the tangential surface velocity versus normalized arclength for different values of  $C_\infty$  with other parameters fixed as above, i.e.  $\lambda = 0$ ,  $Bi' = \infty$ ,  $E = 0.2$ , and  $\Gamma_0 = K/(1 + K)$ . Here, the capillary number  $Ca_e = \mu_2 U_G / \gamma_e$  based on the equilibrium surface tension  $\gamma_e = 1 + E \log(1 - \Gamma_0)$  is taken to be fixed at  $Ca_e = 0.04$ , so that the shape and deformation of the bubble is nearly constant as  $C_\infty$  and hence  $\gamma_e$  varies. The data show that the mobility of the interface, as measured by the interface velocity, decreases initially as  $K$  increases from zero, until  $K \simeq 1.5$ .

However, further increase of  $C_\infty$  causes the opposite to occur, that is, the surface remobilizes and  $u_s$  increases with further increase of  $K$ . At high bulk concentrations the interface becomes saturated with surfactant, and this mitigates the advective accumulation at the endpoints and reduces the gradient in  $\Gamma$ . We note that a similar effect occurs for a spherical gas bubble rising steadily in a fluid with soluble surfactant, where an increased rise velocity of a surfactant retarded bubble is observed at sufficiently high bulk concentration [45].

A scaling relation that explains that explains this behavior is given in Appendix A, following Wang et al. [45]. Their result is adapted to the limit  $Pe' \rightarrow \infty$  based on the reduced equation (17) for bulk surfactant transport in the transition layer. This gives a dimensionless Marangoni stress  $\partial\gamma/\partial s$  in terms of the elasticity number  $E$ , equilibrium partition coefficient  $K$ , and the fixed quantity  $Q = J'_0/K$  as

$$\tau_m \simeq \frac{E}{Q} \frac{K}{(1 + K)^2}. \quad (30)$$

When  $K \rightarrow 0$ ,  $\tau_m \sim EK/Q$ , and as  $K \rightarrow \infty$ ,  $\tau_m \sim E/(QK)$  and again tends to zero. We note that the surface concentration  $\Gamma$  approaches one as  $K$  becomes large, and it at first appears that with the nonlinear equation of state (6) the Marangoni stress  $d\gamma/ds = E/(1 - \Gamma)(d\Gamma/ds)$

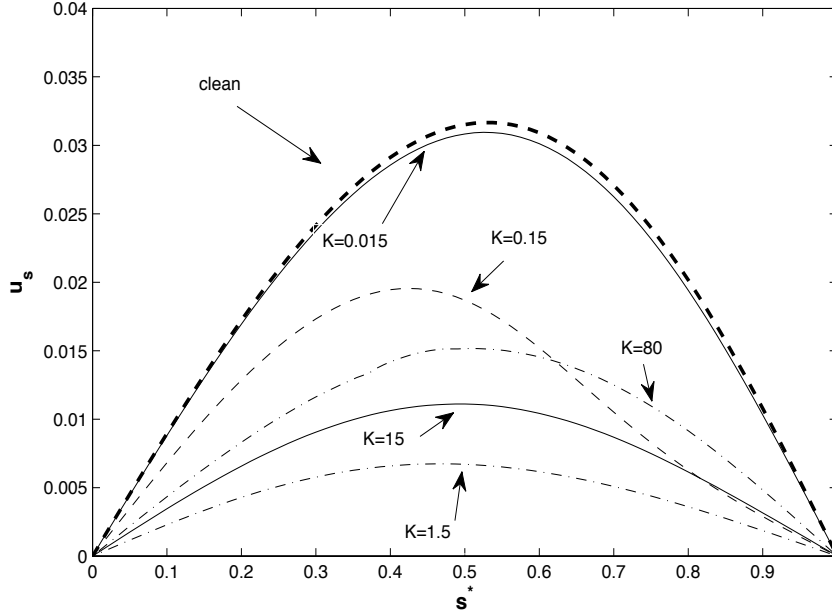


FIG. 8: Tangential component of surface velocity  $u_s$  versus normalized arclength  $s^*$ , for varying bulk concentration  $C_\infty$ . The ratio  $J'_0/K = 15$  is fixed,  $Ca_e = 0.04$ , and other fixed parameter values are given in the text.

diverges in this limit. However, the result (30) and our numerical simulations reflect the fact that the surfactant concentration gradient  $d\Gamma/ds$  on the surface tends to zero sufficiently fast that the Marangoni stress also tends to zero.

### C. Transient deformation for $Bi' = \infty$

Figure 9 gives an example of the transient deformation of a slightly viscous drop in a pure strain flow when the capillary number is greater than the critical value for bursting. Parameter values here are  $\lambda = 0.025$ ,  $E = 0.2$ ,  $K = 1.5$  ( $\Gamma_0 = K/(1 + K)$ ),  $J'_0 = 0.03$  and  $Ca = 0.176$  and are chosen to be comparable to those used in the transient simulations for arbitrary  $Bi'$  in section IV D. The drop evolves to a transient, nearly pointed shape and soon thereafter emits a small droplet from each endpoint. This shows that a type of tipstreaming can occur in the diffusion controlled regime  $Bi' = \infty$  but the tip streams without the simultaneous formation of a long thin thread.

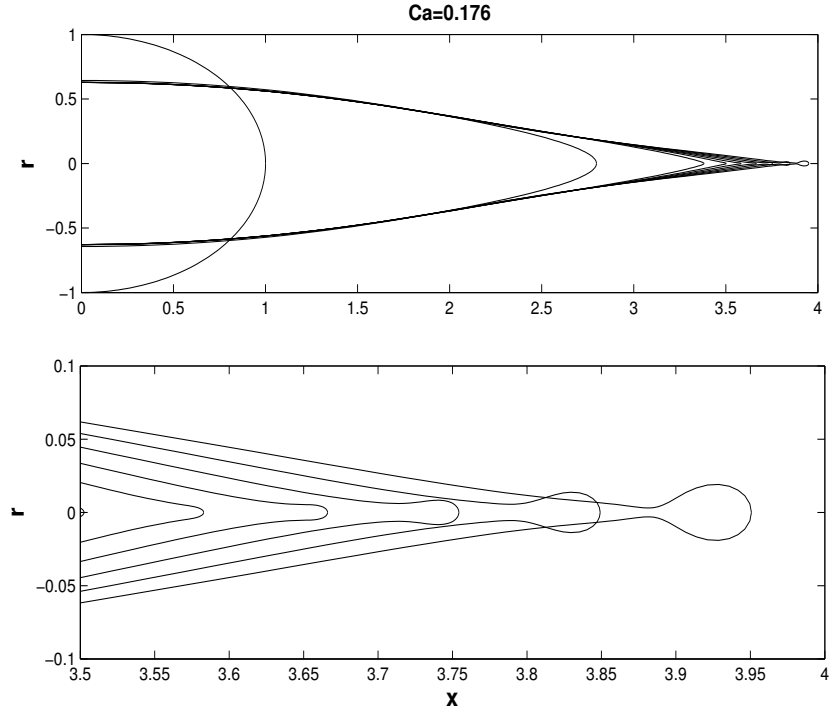


FIG. 9: An example of tipstreaming when  $Bi' = \infty$ . Parameter values are given in the text. The lower panel shows a magnified view of the drop tip.

#### D. Steady and transient deformation for $0 < \lambda \ll 1$ and varying $Bi'$

The steady deformation studied in the previous section assumed that the interface kinetics are in the diffusion-controlled limit  $Bi' = \infty$ . The hybrid numerical method developed here also allows the investigation of interface dynamics and effects of surfactant solubility over the full range of Biot number. Figure 10 examines the effect of varying the Biot number  $Bi'$  on unsteady deformation and tipstreaming, with other parameters the same as in §IV C except for the capillary number, which is reduced to  $Ca = 0.127$ . The upper panel of the figure compares the shapes of tipstreaming filaments for soluble surfactant with  $Bi' = 2.0, 0.2, 0.02$  and for insoluble surfactant, when  $Bi' = 0$ . When  $Bi' = 0$  the boundary condition (19) implies  $\partial C/\partial N' = 0$  on the interface, so that from equation (21) there is no effect of surfactant solubility. The interface profiles are plotted at a time near pinch-off, when a small droplet is about to be emitted at the tip. The dashed profiles show steady solutions at the same  $Ca$  for both a clean drop and when  $Bi' = 200$ . At this capillary

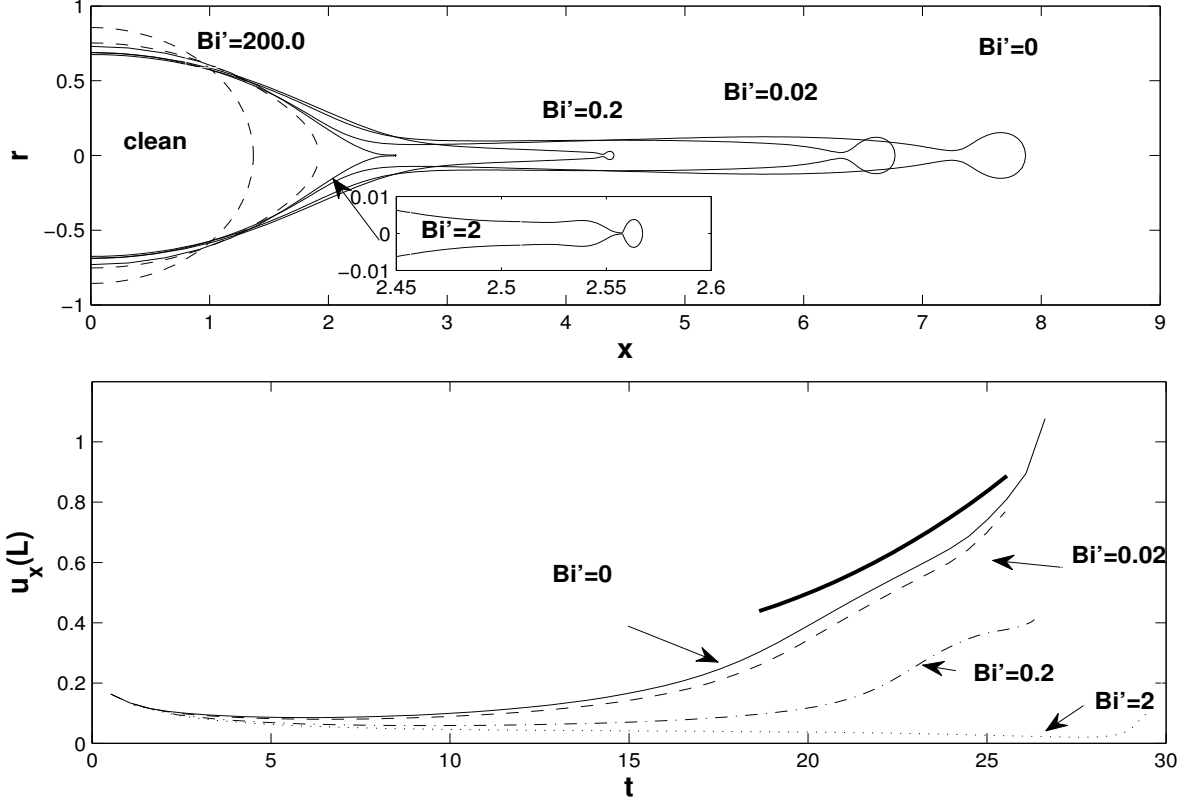


FIG. 10: Tipstreaming for indicated values of the Biot number  $Bi'$ . Parameter values are  $\lambda = 0.025$ ,  $E = 0.2$ ,  $K = 1.5$ ,  $\Gamma_0 = 0.6$ ,  $J'_0 = 0.03$ , and  $Ca = 0.127$ . The dashed profiles are steady-state solutions for a clean bubble and for  $Bi' = 200$ . The solid profiles are shown at times  $t = 29.6, 26.3, 26.0$  and  $26.6$  for  $Bi'$  decreasing from 2.0 to 0 (the insoluble limit). The inset shows details of the  $Bi' = 2.0$  solution where a highly-adaptive grid is used to resolve fine details of the shape.

number, tipstreaming is not observed when  $Bi' = 200$  but does occur at higher  $Ca$ .

The figure shows that as  $Bi'$  increases from 0.02 to 2.0, the tipstreaming filaments become shorter and thinner. Axial velocities  $u_x(L(t))$  at the advecting filament tips, where  $x = L(t)$  is the location of the drop tip, decrease with increasing  $Bi'$  as shown in the lower panel of the figure.

The short thick line in the lower panel denotes  $u_x(L(t)) = Ca L(t)$  which is the velocity of a drop tip that moves with the imposed extensional flow  $u'_x = Ca x$ . This is the asymptotic result derived in [6] using slender body theory when  $\lambda = 0$  and the surfactant is insoluble.

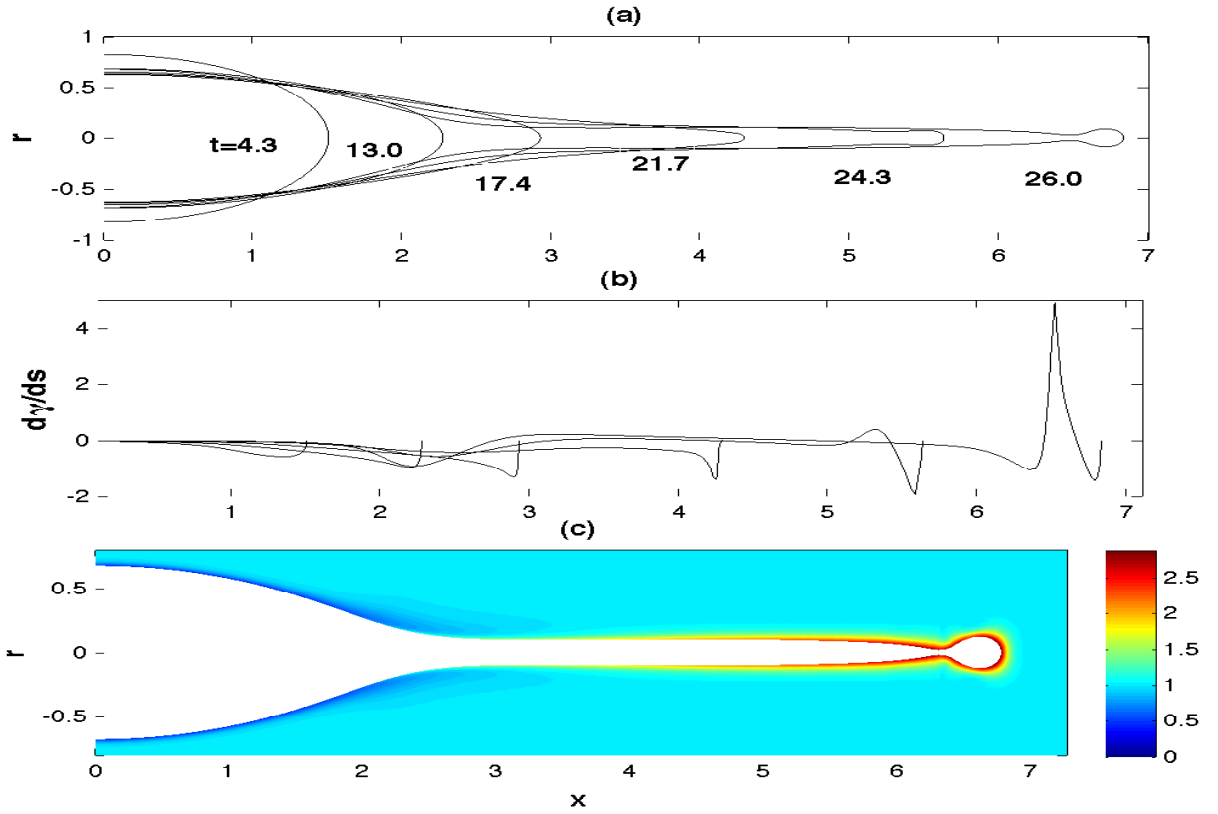


FIG. 11: (a) Time-evolution of a tip streaming filament when  $Bi' = 0.02$  shown at the indicated times. Other parameters are as in Figure 10. (b) Marangoni stress  $d\gamma/ds$  versus axial position  $x$  at the same sequence of times. (c) Instantaneous bulk surfactant concentration at  $t = 26$ .

The computed velocity for insoluble surfactant with  $\lambda = 0.025$ , given by the thin solid curve, is close to this result.

Figure 11(a) presents snapshots of the time evolving drop shape when  $Bi' = 0.02$  together with the Marangoni stress  $d\gamma/ds$  on the surface when  $x > 0$  in Figure 11(b). This shows a strong localized Marangoni stress directed opposite to the imposed flow ( $d\gamma/ds < 0$ ) that develops on the side of the thread immediately behind the drop tip or endpoint. This part of the interface behaves like a no-slip surface, and is dragged or advected at a velocity close to that of the imposed flow. Note that there is also a relatively large positive Marangoni stress ( $d\gamma/ds > 0$ ) that develops a little further behind the drop tip at late times, and this is believed to be related to the onset of pinchoff near the drop tip.

The decreasing thread thickness and tip velocity of the tipstreaming filaments with in-

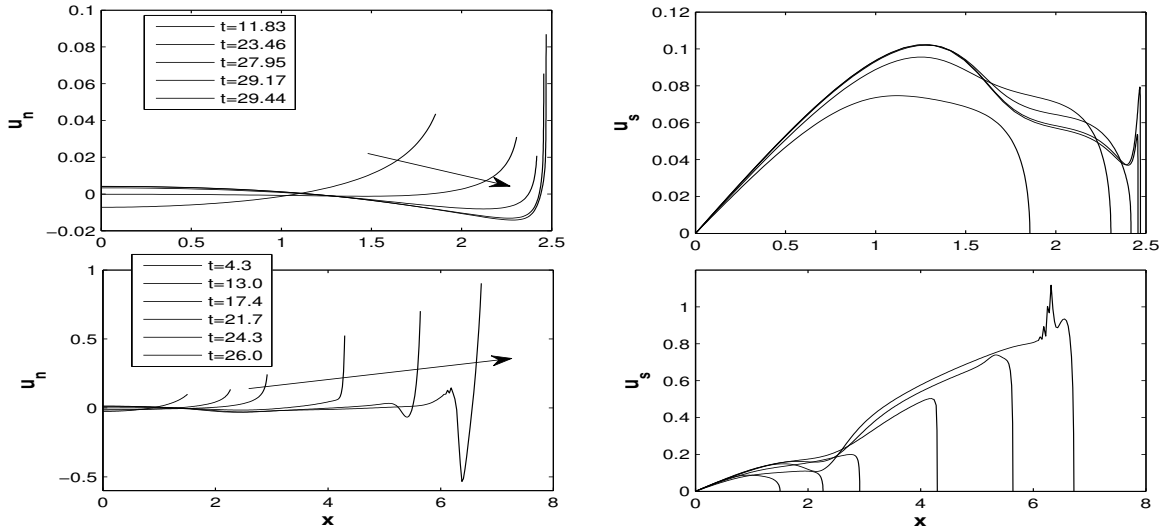


FIG. 12: Normal and tangential components of velocity  $u_n$ ,  $u_s$  on the drop interface at axial position  $x > 0$ , for the  $Bi' = 2.0$  (top panels) and  $Bi' = 0.02$  (bottom panels) evolution of Figure 10 at the indicated times. The drop tip corresponds to the right endpoint of the curves. (Note that  $u_s = 0$  at the tip).

creasing  $Bi'$  is explained as follows. As  $Bi'$  is increased with  $K$  and  $J'_0$  fixed the rate of interface kinetics for surfactant exchange increases relative to the capillary flow rate, and there is enhanced transport of surfactant via solubility from the drop tip, where the surface concentration  $\Gamma$  is highest, to the bulk fluid. The interface and interfacial surfactant are remobilized near the drop tip, which reduces the Marangoni-induced drag force. This remobilization is illustrated in Figure 12 (top panels), which shows that at the relatively large value  $Bi' = 2.0$  the tangential fluid velocity at the drop surface just behind the tip is for a short time interval just before pinch-off much greater than the normal tip velocity, see the leftmost three curves. During this phase (phase one) the drop evolves to a nearly steady pointed shape over much of its surface, but the imposed flow subsequently stretches the surface in a small neighborhood of the tip where the drag force is greatest. In this second phase the tangential fluid velocity on the drop interface near the tip approaches the normal tip velocity, i.e., the drop surface briefly becomes immobilized, and a thin filament is emitted, see the rightmost two curves (top panels) and the inset of Figure 10 at  $Bi' = 2.0$ . We note that similar dynamics are sometimes observed for sufficiently small initial interfacial surfactant concentration  $\Gamma_0$  at other values of  $Bi'$ , when a small immobilized region develops

near a sharp drop tip, which facilitates the tipstreaming of a very thin thread. Figure 13 shows the time evolution when  $Bi' = 2.0$  during both phases.

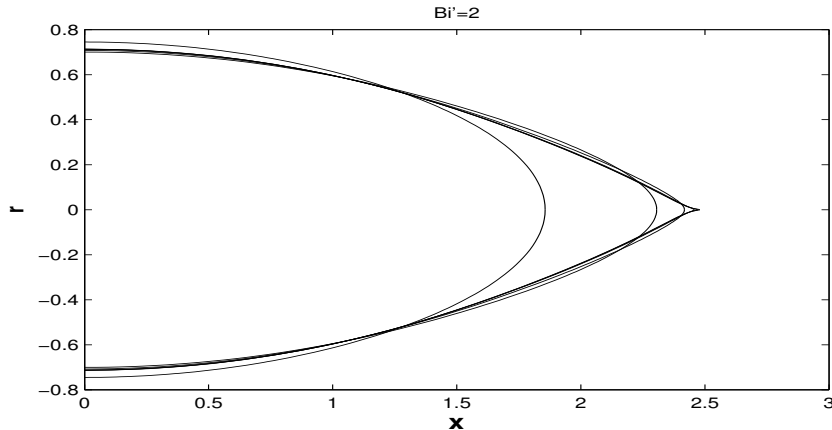


FIG. 13: Time-evolution of interface profiles for the drop of Figure 10 when  $Bi' = 2.0$ . The profiles are shown at the same times as in the upper panels of Figure 12, prior to formation of the tipstreaming thin filament shown in the inset of of Figure 10.

At the much smaller value  $Bi' = 0.02$ , the tangential fluid velocity near the drop tip is always comparable to the normal tip velocity, as shown in the bottom panels of Figure 12. The dynamics are more like that for a drop with insoluble surfactant and an immobile surface. The evolving drop shapes are more rounded at the tips, and the resulting tipstreaming filament is thicker. A simple explanation for the change in radius of the tipstreaming thread with  $Bi'$  is based on the normal stress balance at the interface, which is close to equilibrium so that the Laplace-Young relation  $\Delta p = \gamma/R$  is a good approximation, where  $\Delta p$  is the pressure difference across the interface and  $R$  is the thread radius. For a nearly inviscid thread  $\Delta p$  is almost constant along its length. When  $Bi' = 2.0$  the surface surfactant concentration on the short tipstreaming thread is close to the maximum packing concentration everywhere, so that the surface tension  $\gamma$  is small and this is in near-equilibrium with a small thread radius. When  $Bi' = 0.02$ , the longer thread is stretched axially by the imposed flow, which dilutes the surface surfactant concentration, leading to a larger surface tension and near-equilibrium with a larger thread radius.

### E. Conditions for tipstreaming

The quantities that are most easily varied in experiments on drop breakup with soluble surfactant are the bulk concentration at infinity  $C_\infty$  and the imposed flow speed  $U_G = G R_0$ . Moyle et al. present a phase or operating diagram for drop breakup in their microfluidic experiment [29], [3] by plotting a dimensionless ambient concentration  $\overline{C}$  versus flow rate  $\overline{Q}$  at which various breakup modes, including tipstreaming, occur. Although the confined, flow-focussing geometry of the microfluidic experiment differs from the unbounded geometry considered here it is informative to construct a similar diagram.

In the microfluidic experiment [29], [3], which was summarized in §I, the geometry and fluid system are fixed with length scale  $R_0 = 90 \mu\text{m}$  equal to the radius of the dispersed phase feed or capillary tube, external fluid viscosity  $\mu_2 = 40 \text{ mPa s}$ , viscosity ratio  $\lambda = 0.025$ , and clean surface tension  $\gamma_0 = 62.5 \text{ mN m}^{-1}$ . Three surfactants,  $C_{10}E_8$ ,  $C_{12}E_8$ , and  $C_{14}E_8$  are tested and give nearly identical conditions for tipstreaming [29]. Measurements on these surfactants give  $\Gamma_\infty = 2.25 \mu\text{mol m}^{-2}$  and adsorption rate  $\kappa_a \simeq 22 \text{ m}^3 \text{ mol}^{-1} \text{ s}^{-1}$  for all three surfactants while they differ greatly in their desorption rates, which are  $\kappa_d = 2.5 \times 10^{-2} \text{ s}^{-1}$  for  $C_{10}E_8$ ,  $6.8 \times 10^{-6} \text{ s}^{-1}$  for  $C_{12}E_8$  and  $2.5 \times 10^{-8} \text{ s}^{-1}$  for  $C_{14}E_8$ . A large range of bulk concentration of surfactant is used in the experiments, varying from one-tenth to fifteen times the critical micelle concentration (CMC) of  $1.0 \times 10^{-4} \text{ mol l}^{-1}$ , and the bulk diffusivity is  $D \simeq 10^{-10} \text{ m}^2 \text{ s}^{-1}$  [31]. The elasticity number is estimated to be  $E \simeq 0.10$ . The imposed fluid velocity is of the order of  $10^{-2}$  to  $1 \text{ m s}^{-1}$ . With these values we estimate  $Pe' \simeq 10^6$ ,  $Bi' \simeq 10^{-12}$  to  $10^{-6}$ ,  $K \simeq 10^2$  to  $10^8$ ,  $J' \simeq 10^{-6}$ . The dimensionless group  $Bi'/J'$  of subsection II A that is to be a small parameter in the sorption-controlled regime is in the range from 1.0 to  $10^{-6}$ , while the group  $Bi'/J'_0$  relevant to the sorption-controlled regime in the large Peclet number limit is smaller by a factor of  $10^{-3}$ . On its own, this suggests that the experiments are conducted in the sorption-controlled regime, for which bulk concentration gradients are less important to the dynamics. However, the pseudo solubility model is a fast bulk diffusion limit ( $J' \rightarrow \infty$  with  $Bi'$  fixed), which is not consistent with large values of  $Pe'$ . Given the large value of  $Pe'$ , and the size and range of  $Bi'$  and  $K$ , the simulations are conducted using the hybrid numerical method and the mixed kinetic boundary condition (19).

Definitions of the dimensionless ambient bulk surfactant concentration and imposed flow

rate that are analogous to those given in [29], [3] are

$$\bar{C} = \frac{\mu_2 R_0 \kappa_a C_\infty}{RT\Gamma_\infty} = \frac{Bi'K}{E} \quad \text{and} \quad \bar{Q} = \frac{\mu_2 U_G}{RT\Gamma_\infty} = \frac{Ca}{E}. \quad (31)$$

Figure 14 presents a phase diagram based on our numerical data that gives conditions for tipstreaming and other breakup modes in terms of  $\bar{C}$  and  $\bar{Q}$ . The experimentally relevant parameter  $C_\infty$  is changed with other parameters held fixed by varying  $J'_0$  and  $K$  when  $J'_0/K$  is fixed. We set  $\lambda = 0.025$  and  $E = 0.15$ , which are comparable to the experimental values, and  $Bi' = 2 \times 10^{-4}$ , which is at the upper end of the experimental range.

In the figure, conditions that lead to tipstreaming are denoted by ‘×’, and conditions that produce a steady state drop shape are denoted by ‘o’. At relatively large dimensionless ambient concentration and flow rate we observe a different breakup mode, denoted by ‘+’. This mode is distinguished by a drop shape that has a gradual decrease in radius  $r$  and a gradual increase in surface surfactant concentration  $\Gamma$  with increasing axial coordinate  $x$ . A representative example of this stretching profile with  $\bar{C} = 0.0067$  and  $\bar{Q} = 2.0$  is shown in Figure 15 and it does not exhibit the thin filament or thread that is characteristic of tipstreaming. We expect the region in phase space for this breakup mode to extend to yet higher ambient concentration  $\bar{C}$  and flow rate  $\bar{Q}$  in the upper right portion of the plot. However, the computations require an increasingly small timestep at larger  $\bar{C}$  and  $\bar{Q}$ .

The plot in Figure 14 is for a fixed Biot number  $Bi' = 2 \times 10^{-4}$ , and calculations at other  $Bi'$  show a slight dependence on this parameter. For example, when  $Bi'$  is increased to 0.02 the phase diagram is similar to that of Figure 14 but where the regions of the various breakup modes are translated upward and to the right.

Comparison of Figure 14 with the equivalent Figure 7 of [29] shows a broad similarity in the location of the tipstreaming region, which in the experiments occurs for dimensionless flow rate  $10^{-1} < \bar{Q} < 10^0$  and concentration  $10^{-4} < \bar{C} < 10^{-2}$ . However, there are some important differences to be noted when making a comparison. First, some of the boundaries of the tipstreaming region in the experiments are ascribed to constraints imposed by its confined geometry, which do not pertain here. Secondly, in the experiments of Moyle et al. surfactant is continually fed to the interface so as to sustain tipstreaming over time. In contrast, we consider transient tipstreaming from a drop interface that is initially spherical and at equilibrium. Simulation of tipstreaming dynamics in a confined geometry is beyond the scope of the current paper, and will be considered in future work. Given the difference

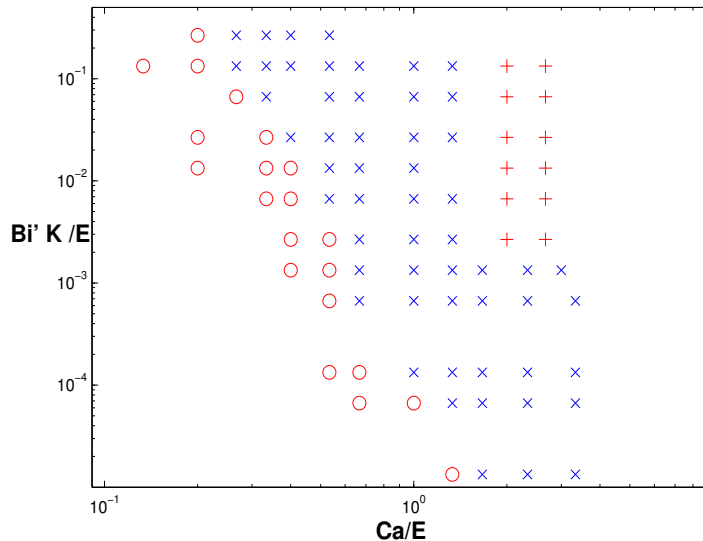


FIG. 14: Conditions for tipstreaming and other breakup modes in terms of the dimensionless concentration  $\overline{C}$  and flow rate  $\overline{Q}$  (note log-log scales). The ‘o’ markers denote steady-state drop shapes, ‘x’ markers denote tipstreaming drops, and ‘+’ markers denote a nontipstreaming breakup mode. Fixed parameters are  $\lambda = 0.025$ ,  $E = 0.15$ , and  $Bi' = 2 \times 10^{-4}$ .

between the experiments and the simulations reported here, we believe the agreement in the location of the tipstreaming region is surprisingly good.

## V. CONCLUSIONS

Numerical computations have been presented using a hybrid numerical method for interfacial flow with soluble surfactant in the infinite bulk Peclet number limit. The method was introduced for 2D flow in [6], [47], and has been adapted here to treat 3D axisymmetric flow and to incorporate the mixed-kinetic boundary condition (9) that holds for arbitrary Biot number  $Bi'$ . The method also has improved resolution of the transition layer structure near stagnation points on the interface by using a modified far-field matching condition (27). The algorithm accurately resolves the transition layer adjacent to the interface that occurs at large bulk Peclet number, across which the surfactant concentration may vary rapidly. The behavior in the transition layer is found by a singular perturbation analysis of the governing equations near the interface  $S$  in the limit  $Pe' \rightarrow \infty$ . This uses an intrinsic, surface fitted coordinate frame in terms of which a reduced equation (17) governs the transport of bulk

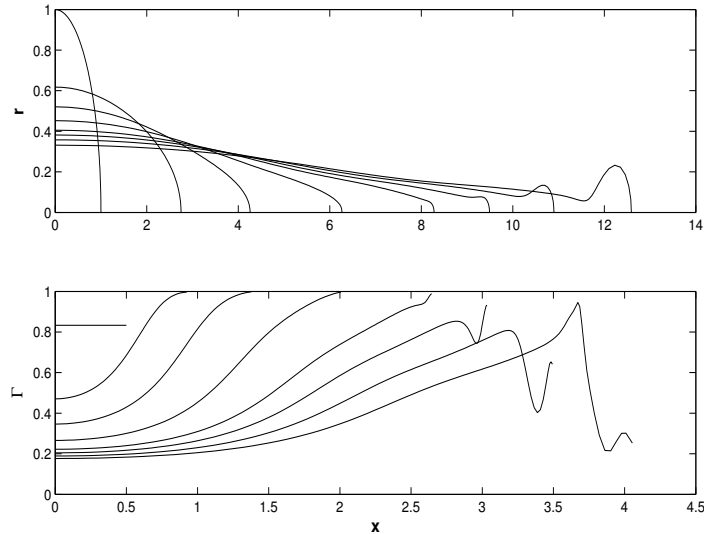


FIG. 15: Example of a nontipsteaming mode of breakup denoted by a ‘+’ in Figure 14. Time-evolution of interface shapes (top) at times  $t = 0.0, 3.9, 4.4, 5.2, 6.4, 7.4, 7.9, 8.4$  and interfacial surfactant concentration  $\Gamma$  (bottom).

concentration within the layer, subject to boundary conditions (19) on  $S$  and (27) in the far field. Our implementation of the hybrid numerical method combines a numerical solution of the boundary value problem for  $C$  in the intrinsic coordinate frame with a boundary integral solution for surface quantities  $\mathbf{u}_s$  and  $\Gamma$ . The numerical method has been validated by application to various test problems.

This study has focussed on application of the hybrid numerical method to investigate the effect of soluble surfactant on the deformation and breakup of a single drop or bubble stretched in a uniaxial extension flow of a viscous fluid. We have considered the effect of soluble surfactant on steady-state solution branches for inviscid bubbles with  $\lambda = 0$  in the diffusion controlled regime  $Bi' = \infty$ , in which the surfactant exchange kinetics are in equilibrium. Two parameters control the effects of surfactant solubility in this regime: the transfer coefficient  $J'_0$ , and the partition coefficient for the relative rate of adsorption to desorption  $K$ . We find that increasing  $J'_0$  or decreasing  $K$ , with other parameters held fixed, raises the efficiency of surfactant desorption relative to adsorption, and allows for greater slip velocities at the interface. In this case the interface evolves as though it is more nearly surfactant-free. In the opposite limits (i.e., decreasing  $J'_0$  or increasing  $K$ ) the behavior of

an insoluble surfactant is recovered.

We have also examined the effect of varying the ambient bulk concentration of surfactant. At high bulk concentration  $C_\infty$ , we find that the interface velocity ‘remobilizes’ or tends toward the surfactant-free velocity. This effect is similar to that which occurs for a steadily rising gas bubble at a large concentration of bulk surfactant.

Our numerical method is also able to compute resolved examples of tipstreaming drops with soluble surfactant, and we have characterized the dependence of tipstreaming threads or filaments on parameters, notably the Biot number  $Bi'$ . We show that tipstreaming filaments become thinner with increasing  $Bi'$ , which suggests a means to control the size of droplets that are formed when the thread breaks up. We also present a phase diagram which gives conditions or parameter values for tipstreaming in the context of an unbounded geometry and compare with a similar diagram that has been obtained from the microfluidic experiments of [3].

There are several ways to generalize the hybrid numerical method that is described here. The method is not limited to zero Reynolds number flow, and numerical methods that are designed to solve for moving interfaces in Navier-Stokes flow at moderate Reynolds numbers, such as the immersed interface or level set method, can be combined with equation (17) to accurately capture the dynamics of the  $Pe' = \infty$  transition layer. We have considered examples where the bulk surfactant distribution far from the drop is spatially uniform, but the method can be extended to include the case where this is nonuniform. The bulk concentration outside the transition layer can be tracked by, for example, a semi-Lagrangian method using a relatively coarse grid.

## VI. APPENDIX

### A. Derivation of the scaling relation for Marangoni stress

The scaling relation (30) for the dimensionless Marangoni stress  $\tau_m = d\gamma/ds$  is derived following [45]. A characteristic scale for the variation in bulk concentration  $\Delta C$  is obtained by balancing surface advection  $U\Gamma_\infty\Gamma_0/R_0$  with bulk diffusion  $DC_\infty\Delta C/\epsilon R_0$ , which gives

$$\Delta C \simeq \frac{U\Gamma_\infty\Gamma_0\epsilon}{DC_\infty} = \frac{\epsilon}{J'} \frac{K}{K+1}. \quad (32)$$

Here  $\Gamma_0 = K/(K + 1)$  is the equilibrium surface concentration of surfactant (per (12)) and  $U = U_\gamma = \gamma_0/\mu_2$  is the capillary velocity scale, and note that the undisturbed drop radius  $R_0$  is used as a length scale in the tangential interface direction while the transition layer width  $\epsilon R_0$  is used in the normal direction. The scale for the dimensionless Marangoni stress is

$$\tau_m \simeq \frac{\partial\gamma}{\partial\Gamma}\Big|_{\Gamma_0} \Delta\Gamma \simeq \frac{E}{1 - \Gamma_0} \Delta\Gamma \quad (33)$$

using  $\frac{\partial\gamma}{\partial\Gamma}\Big|_{\Gamma_0} = -\frac{E}{1 - \Gamma_0}$ , which follows from the surface equation of state (6). A relation between  $\Delta\Gamma$  and  $\Delta C$  is obtained by taking the variation of the equilibrium adsorption isotherm (13), which shows that  $\Delta\Gamma = K(1 - \Gamma)\Delta C/(1 + KC)$ . Substitution of (32),  $\Gamma \simeq \Gamma_0 = K/(1 + K)$ , and  $C \simeq 1$  into this expression gives

$$\Delta\Gamma \simeq \frac{K^2}{(1 + K)^3} \frac{\epsilon}{J'}. \quad (34)$$

The scaling relation for the dimensionless Marangoni stress (30) then follows from insertion of (12), (34) and  $Q = J'/\epsilon K$  into (33).

### B. Steady solution for $Ca \ll 1$

A steady solution in the limit of small capillary number can be found by setting  $E = 0$  and  $C|_S = 0$ . When  $E = 0$ , the surface tension  $\sigma = 1$  and the coupling from the evolution of interfacial and bulk surfactant concentrations to the underlying flow is removed. In the small capillary number limit the drop is only slightly deformed, and an expansion for the flow field and perturbed drop shape has been given by, for example, Stone and Leal [38]. With the boundary condition  $C|_S = 0$ , the coupling from the interfacial to the bulk surfactant phase is also removed, and the drop surface is a perfect sink for bulk surfactant. A solution in the context of a 2D inviscid bubble was given in this limit in [7].

The velocity and pressure in the interior and exterior regions are given by Lamb's general solution [23]. In an imposed strain with strain-rate tensor  $\mathbf{E}$  and no imposed vorticity, these

are

$$\begin{aligned}
\mathbf{u}'_2 &= Ca \left( \mathbf{E} \cdot \mathbf{x} + \frac{c_2}{r^5} \left[ 2\mathbf{E} \cdot \mathbf{x} - 5\mathbf{x} \frac{\mathbf{x} \cdot \mathbf{E} \cdot \mathbf{x}}{r^2} \right] + c_3 \mathbf{x} \frac{\mathbf{x} \cdot \mathbf{E} \cdot \mathbf{x}}{r^5} \right) + O(Ca^2), \\
p'_2 &= p_\infty + Ca \left( 2c_3 \frac{\mathbf{x} \cdot \mathbf{E} \cdot \mathbf{x}}{r^5} \right) + O(Ca^2), \\
\mathbf{u}'_1 &= Ca (2\hat{c}_2 \mathbf{E} \cdot \mathbf{x} + \hat{c}_3 [5r^2 \mathbf{E} \cdot \mathbf{x} - 2\mathbf{x}(\mathbf{x} \cdot \mathbf{E} \cdot \mathbf{x})]) + O(Ca^2), \\
p'_1 &= p_0 + Ca (21\hat{c}_3 \mathbf{x} \cdot \mathbf{E} \cdot \mathbf{x}) + O(Ca^2).
\end{aligned}$$

The conditions of zero normal velocity, continuity of tangential velocity, and continuity of tangential stress evaluated at leading order, on  $r = |\mathbf{x}| = 1$ , give

$$c_2 = \frac{-\lambda}{2(1+\lambda)}, \quad c_3 = \frac{-(2+5\lambda)}{2(1+\lambda)}, \quad \hat{c}_2 = \frac{-3}{4(1+\lambda)}, \quad \hat{c}_3 = \frac{1}{2(1+\lambda)}$$

(per [38], at equations (A11) and (A12) in the steady state with  $b_\Gamma = 0$ , and the first of equations (A10)). The normal stress balance gives the pressure difference  $p_0 - p_\infty = 2$  at leading order, and gives the correction to the drop shape at order  $O(Ca)$ , which is

$$r = 1 + Ca \frac{(16+19\lambda)}{8(1+\lambda)} \frac{\mathbf{x} \cdot \mathbf{E} \cdot \mathbf{x}}{r^2} + O(Ca^2)$$

in the steady state (per [38], equation (A14) with  $b_\Gamma = 0$ ).

For the uniaxial extension, the strain-rate tensor is

$$\mathbf{E} = \begin{pmatrix} -\frac{1}{2} & 0 & 0 \\ 0 & -\frac{1}{2} & 0 \\ 0 & 0 & 1 \end{pmatrix},$$

so that the surface velocity is

$$\mathbf{u}_S = -\frac{3Ca}{4(1+\lambda)} \sin 2\phi \mathbf{e}_\phi \quad (35)$$

which has surface divergence  $\nabla_S \cdot \mathbf{u}_S = (-3Ca/(4(1+\lambda)))(1+3\cos 2\phi)$ , where  $\phi \in [0, \pi]$  is the angle of declination from the axis of extension. With an origin of surface coordinates at the drop pole  $\phi = 0$ ,  $\mathbf{U}_S = 0$ , and the transition layer equation (25) becomes

$$\frac{3Ca}{4(1+\lambda)} \left( -\sin 2\phi \frac{\partial C}{\partial \phi} + (1+3\cos 2\phi)N \frac{\partial C}{\partial N} \right) = \frac{\partial^2 C}{\partial N^2} \quad (36)$$

to leading order in  $Ca$ .

We look for a similarity solution  $C = C(\eta)$  of (36), where the similarity variable is

$$\eta = \left( \frac{3Ca}{4(1+\lambda)} \right)^{1/2} \frac{N}{g(\xi)} \quad \text{and} \quad \xi = \cos 2\phi.$$

Then (36) implies that

$$C_{\eta\eta} = -2\eta C_{\eta} \quad \text{and} \quad (1 - \xi^2)gg' - \frac{1}{2}(1 + 3\xi)g^2 = 1.$$

The boundary conditions for  $C$  require that  $C = 0$  when  $\eta = 0$  and  $C \rightarrow 1$  as  $\eta \rightarrow \infty$ . The general solution for  $g(\xi)$  is singular at the drop poles  $\phi = 0, \pi$  and at the equator  $\phi = \pi/2$ , but an integration constant can be chosen to find a solution that is bounded at the equator, at which the imposed flow is incoming. This gives

$$C(\eta) = \text{erf}(\eta) \quad \text{where} \quad \eta = \left( \frac{3Ca}{4(1+\lambda)} \right)^{1/2} \frac{N \sin \phi}{(1 - \frac{1}{2} \cos^2 \phi)^{1/2}} \quad (37)$$

and  $\text{erf}(\eta) = (2/\sqrt{\pi}) \int_0^\eta e^{-u^2} du$  is the error function. This solution is such that at the drop poles  $\phi = 0, \pi$ ,  $C(N) = 0$  for all  $N$ , which is consistent with the flow leaving the steady drop surface there.

- 
- [1] A. Acrivos and T. S. Lo. Deformation and breakup of a single slender drop in an extensional flow. *J. Fluid Mech.*, 86:641–672, 1978.
  - [2] A. Acrivos and J. M. Rallison. A numerical study of the deformation and burst of a viscous drop in an extensional flow. *J. Fluid Mech.*, 89:191–200, 1978.
  - [3] Shelley L. Anna and Hans C. Mayer. Microscale tipstreaming in a microfluidic flow focusing device. *Phys.Fluids*, 18:121512, 2006.
  - [4] D. Barthes-Biesel and A. Acrivos. Deformation and burst of a liquid droplet freely suspended in a linear shear field. *J. Fluid Mech.*, 61:1–21, 1973.
  - [5] I. B. Bazhlekov, P. D. Anderson, and H. E. H. Meijer. Numerical investigation of the effect of insoluble surfactants on drop deformation and breakup in simple shear flow. *J. Colloid Interface Sci.*, 298:369–394, 2006.
  - [6] M. R. Booty and M. Siegel. Steady deformation and tip-streaming bubble with surfactant. *J. Fluid Mech.*, 544:243–275, 2005.
  - [7] M. R. Booty and M. Siegel. A hybrid numerical method for interface fluid flow with soluble surfactant. *J. Comp. Phys.*, 229:3864–3883, 2010.

- [8] J. D. Buckmaster. Pointed bubbles in slow viscous flow. *J. Fluid Mech.*, 55:385–400, 1972.
- [9] C.-H. Chang and E. I. Franses. Adsorption dynamics of surfactants at the air/water interface: a critical review of mathematical models, data, and mechanisms. *Coll. Surf. A: Physico Eng. Asp.*, 100:1–45, 1995.
- [10] K. Y. Chen and M. C. Lai. A conservative scheme for solving coupled surface-bulk convection-diffusion equations with an application to interfacial flows with soluble surfactant. *Preprint*, 2013.
- [11] R. V. Craster, O. Matar, and D. T. Papageorgiou. Breakup of surfactant-laden jets above the critical micelle concentration. *J. Fluid Mech.*, 629:195–219, 2009.
- [12] R. A. DeBrujin. Tipstreaming of drops in simple shear flows. *Eng. Sci.*, 48 (2):277–284, 1993.
- [13] M. A. Drumright-Clarke and Y. Renardy. The effects of insoluble surfactant at dilute concentration on drop breakup under shear with inertia. *Phys. Fluids*, 16:14, 2004.
- [14] D.A. Edwards, H. Brenner, and D.T. Wasan. *Interfacial Transport Processes and Rheology*. Butterworth-Heinemann, Boston, 1991.
- [15] J. Eggers and S. Courrech du Pont. Numerical analysis of tips in viscous flow. *Phys. Rev. E*, 79:066311, 2009.
- [16] C. D. Eggleton and K. Stebe. An adsorption-desorption-controlled surfactant on a deforming droplet. *J. Coll. Int. Sci.*, 208:68–80, 1998.
- [17] C. D. Eggleton, T. M. Tsai, and K. Stebe. Tip streaming from a drop in the presence of surfactant. *Phys. Rev. Lett.*, 87(4):048302, 2001.
- [18] S. N. Ghadiali, D. Halpern, and D. P. Gaver. A dual-reciprocity boundary element method for evaluating bulk convective transport of surfactant in free-surface flows. *J. Comp. Phys.*, 171:534, 2001.
- [19] J. J. M. Janssen, A. Boon, and W. G. M. Agterof. Influence of dynamic interfacial properties on droplet breakup in simple shear flow. *AIChE J.*, 40:1929–1939, 1994.
- [20] J. J. M. Janssen, A. Boon, and W. G. M. Agterof. Influence of dynamic interfacial properties on droplet breakup in plane hyperbolic flow. *AIChE J.*, 43:1436–1447, 1997.
- [21] F. Jin, N. R. Gupta, and K. J. Stebe. The detachment of a viscous drop in a viscous solution in the presence of a soluble surfactant. *Phys. Fluids*, 18:022103, 2006.
- [22] M. C. A. Kropinski and E. Lushi. Efficient numerical methods for multiple surfactant-coated bubbles in a two-dimensional stokes flow. *J. Comp. Phys.*, 230:4466–4487, 2011.

- [23] H. Lamb. *Hydrodynamics*. Dover, 1945.
- [24] X. F. Li and C. Pozrikidis. The effect of surfactant on drop deformation and on the rheology of dilute emulsion in Stokes flow. *J. Fluid Mech.*, 341:165, 1997.
- [25] Y. Liao and J. B. McLaughlin. Bubble motion in aqueous surfactant solutions. *J. of Colloid and Interface Science*, 224:297–310, 2000.
- [26] J. R. Lister and H. A. Stone. Capillary breakup of a viscous thread surrounded by another viscous fluid. *Phys. Fluids*, 10:2758, 1998.
- [27] W. Milliken and L. G. Leal. The influence of surfactant on the deformation and breakup of a viscous drop: The effect of surfactant solubility. *J. Colloid Interface Sci.*, 166:275–285, 1994.
- [28] W. J. Milliken, H. A. Stone, and L. G. Leal. The effect of surfactant on the transient motion of newtonian drops. *Phys. Fluids A*, 5:69–79, 1993.
- [29] T. M. Moyle, L. M. Walker, and S. L. Anna. Predicting conditions for microscale surfactant mediated tipstreaming. *Phys. Fluids*, 24, 2012.
- [30] M. Muradoglu and G. Tryggvason. A front-tracking method for computation of interfacial flows with soluble surfactants. *J. Comp. Phys.*, 227:2238–2262, 2008.
- [31] R. Palaparthi, D. T. Papageorgiou, and C. Maldarelli. Theory and experiments on the stagnant cap regime in the motion of spherical surfactant-laden bubbles. *J. Fluid Mech.*, 559:1–44, 2006.
- [32] C. Pozrikidis. *Boundary Integral and Singularity Method for Linearized Viscous Flow*. Cambridge University Press, 1992.
- [33] C. Pozrikidis. Numerical studies of cusp formation at fluid interfaces in Stokes flow. *J. Fluid Mech.*, 357:29–57, 1998.
- [34] Y. Y. Renardy, M. Renardy, and V. Cristini. A new volume-of-fluid formulation for surfactants and simulations of drop deformation under shear at a low viscosity ratio. *Eur. J. Mech. B*, 21:49, 2002.
- [35] M. Siegel. Influence of surfactant on rounded and pointed bubbles in two-dimensional stokes flow. *SIAM J. Appl. Math.*, 59:1998–2027, 1999.
- [36] K. Stebe and C. Maldarelli. Remobilizing surfactant retarded fluid particle interfaces. 2 controlling the surface mobility at interfaces of solutions containing surface-active components. *J. Colloid Intl Sciences.*, 163:177–189, 1994.
- [37] H. A. Stone and L. G. Leal. Relaxation and breakup of an initially extended drop in an otherwise quiescent fluid. *J. Fluid Mech.*, 198:399–427, 1989.

- [38] H. A. Stone and L. G. Leal. The effects of surfactants on drop deformation and breakup. *J. Fluid Mech.*, 220:161–186, 1990.
- [39] G. I. Taylor. The formation of emulsions in definable fields of flow. *Proc. Roy. Soc. Lond. A*, 146:501–523, 1934.
- [40] G. I. Taylor. Proceedings of the 11th international congress of theoretical applied mechanics. pages 790–796, Munich, 1964. Springer Verlag, Heidelberg.
- [41] K. E. Teigen, P. Song, J. Lowengrub, and A. Voigt. A diffuse-interface method for two-phase flows with soluble surfactants. *J. Comp. Phys.*, 230(2):375–393, 2011.
- [42] T. M. Tsai and M. J. Miksis. The effects of surfactant of the dynamics of bubble snap-off. *J. Fluid Mech.*, 337:381, 1997.
- [43] R. G. M. van der Sman and S. van der Graaf. Diffuse interface model of surfactant adsorption onto flat and droplet interfaces. *Rheol. Acta*, 46:3–11, 2006.
- [44] Q. Wang. Breakup of a viscous poorly conducting liquid thread subject to a radial electric field at zero reynolds number. *Phys. Fluids*, 24:102102, 24.
- [45] Y. Wang, D. Papageorgiou, and C. Maldarelli. Increased mobility of a surfactant-retarded bubble at high bulk concentrations. *J. Fluid Mech.*, 390:251–270, 1999.
- [46] H. Wong, D. Rumschitzki, and C. Maldarelli. On the surfactant mass balance at a deforming fluid interface. *Phys. Fluids*, 8:3203–3204, 1996.
- [47] K. Xu, M. R. Booty, and M. Siegel. Analytical and computational methods for two-phase flow with soluble surfactant. *SIAM J. Appl. Math.*, 73 (1):572–593, 2013.
- [48] S. Yon and C. Pozrikidis. A finite volume/boundary-element method for flow past interfaces in the presence of surfactants, with application to shear flow past a visous drop. *Computers and Fluids*, 27:879, 1998.
- [49] G. K. Youngren and A. Acrivos. On the shape of a gas bubble in a viscous extensional flow. *J. Fluid Mech.*, 76:433, 1976.
- [50] J. Zhang, D. M. Eckmann, and P. S. Ayyaswamy. A front tracking method for a deformable intravascular bubble in a tube with soluble surfactant transport. *J. Comp. Phys.*, 214:366, 2006.